Cornell NanoScale Science & Technology Facility

Research Experiences for Undergraduates (CNF REU) Program

Global Quantum Leap International Research Training Experience (GQL IRTE) Program

International Research Experiences for Undergraduates (CNF iREU) Program

2022 FINAL REPORTS

Superconducting Coplanar Microwave Resonator

Sean C. Anderson, Jr.

Electrical & Computer Engineering, Morgan State University

Abstract:

We are trying to make on-chip superconducting microwave resonators which are capable of driving spins in semiconductors by using the superconducting metal niobium (Nb). These microwave resonators will work mainly in two ways; Sensing magnetic defects and magnetic order in thin films of new materials; Manipulating and measuring the quantum state of a collection of spin defects for use in quantum technologies. This will aid in the optimization of optics and optoelectronics. In the past, the Rana research group did a similar project with the coplanar microwave waveguide resonator, however, in that experiment, the smaller the dimensions of the metal of the deposited metal, which in that case was copper, then the smaller the extent the magnetic field will radiate outward and there will be greater conductive losses. This is the reason we chose to go with a superconductor, which minimizes conductive losses.

Summary of Research:

This summer research project focused on getting familiar with the cleanroom, learning about what a coplanar microwave resonator is, and aiding in the process of developing one that is superconducting.

The tools we used the most with this project were the AJA sputter deposition system to deposit niobium on a sapphire wafer, along with the ABM contact aligner for the UV exposure to the sapphire wafer, and then development with the Hamatech development tool, which makes the pattern on the sapphire wafer visible using the 726 MlF solution for 60 seconds.

The working principles behind why the device will be resonant at certain frequencies has to do with the transmission lines on the device. A simple analogy can be made with the length of a string where its resonant frequency is directly related to its length by the equation f_o = velocity/2Length, which are considered standing waves.

The same is true of our transmission lines except that in AC electronics, we must consider the voltage and current waves and the rise and collapse of these waves, which will in turn give us a better idea of their resonant frequencies. The inductive and capacitive properties of the superconducting coplanar microwave resonator also gives rise to the resonant frequencies at which the device will operate. Given those two things, transmission line length and the reactive AC components of the device will determine the resonance at which the device operates.

We designed three devices on the sapphire wafer (Figure 1). The respective resonant frequencies of each device are shown in an array on the sapphire wafer and are 2 GHz at 29.62 mm (Figure 2), 4.l GHz at 14.61 mm (Figure 3), and 8 GHz at 7.5 mm (Figure 4).

The idea was to sample materials using the super-conducting coplanar microwave resonator, which entailed probing the resonator with a DC power source

to get a static magnetic field that shoots out perpendicular to the coplanar microwave resonator's surface, and probing the device with a microwave frequency to be sent inside of the device, which created our oscillating magnetic field.

At microwave frequencies, the spin-states of the electrons will split into two even but opposite energies of $El = +1/2\ g\mu_B B$ and $E2 = -1/2\ g\mu_B B$ where $\sim \Delta E = El - E2$.

From there we could observe the electron's spin behaviors from the bode plot that was characterized from the material we sampled and which will be the future work to be performed on this device.

Conclusions and Future Steps:

The device is now ready for characterization, which means that we will next take a look at the transmission characteristics and see where our device is resonant at. Resonance will occur at microwave frequencies where $\hbar(\omega) = g\ \mu_B f;$.

References:

[1]   Standing Waves and Resonance, Chapter 14 - Transmission Lines, Electronics Textbook (allaboutcircuits.com).

[2]   Coplanar waveguide resonators for circuit quantum electrodynamics, Journal of Applied Physics 104, 113904 (2008); https://doi.org/10.1063/1.3010859; M. Göppl, A. Fragner, M. Baur, R. Bianchetti, S. Filipp, J. M. Fink, P. J. Leek, G. Puebla, L. Steffen, and A. Wallraff.
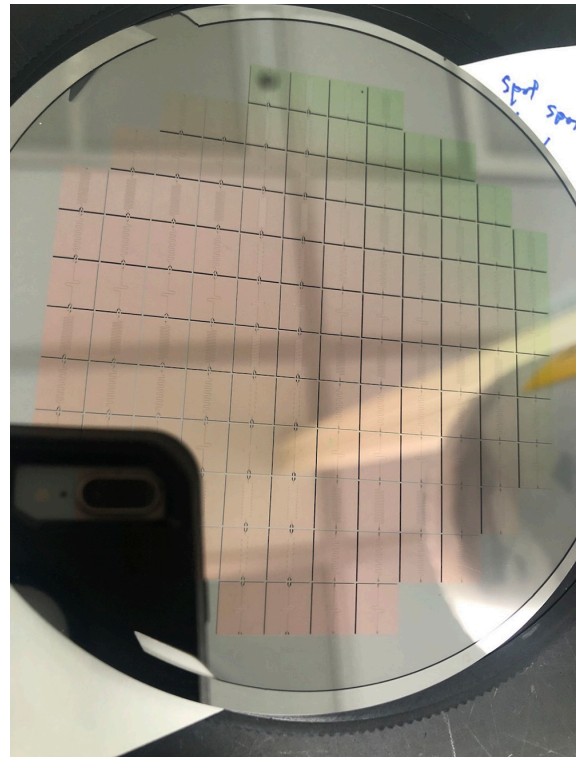
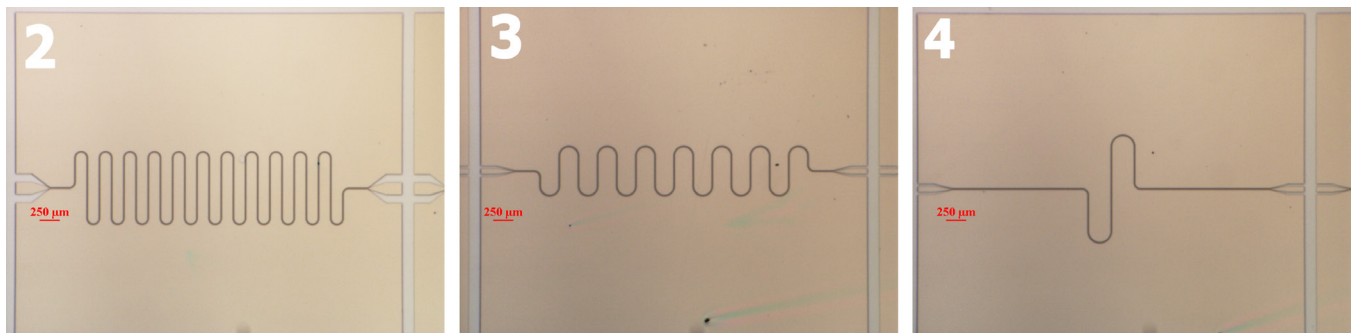*Figure 1: We designed three devices on the sapphire wafer.*

Figure 2-4: The respective resonant frequencies of each device are shown in an array on the sapphire wafer and are 2 GHz at 29.62 mm (Figure 2 left), 4.l GHz at 14.61 mm (Figure 3 middle), and 8 GHz at 7.5 mm (Figure 4 right).

Effect of Different Extracellular Matrix Proteins on Collective Cell Migration

Francesca Marie Bard

Materials Science and Engineering, Cornell University

2022 Cornell NanoScale Science & Technology Facility International Research Experiences for Undergraduates (CNF iREU) Program

CNF iREU Principal Investigator: Dr. Jun Nakanishi, National Institute of Material Science (NIMS), Tsukuba, Ibaraki, Japan

CNF iREU Mentor: Dr. Shimaa A. Abdellatef, NIMS, Tsukuba, Ibaraki, Japan

Primary Source(s) of Research Funding: 2022 CNF iREU Program via NSF grant NNCI-2025233

Contact: fmb54@cornell.edu, NAKANISHI.Jun@nims.go.jp, ABDELALEEM.Shimaa@nims.go.jp

Website: https://cnf.cornell.edu/education/reu/2022

Abstract:

Studying collective cell migration is essential for understanding physiological processes, such as wound healing and cancer metastasis [1]. Since the extracellular matrix (ECM) interacts with cells, through contact guidance and haptotaxis, it is essential to understand how the different ECM proteins affect cell migration patterns [2]. Previous research done in Nakanishi-san's group (by Dr. Shimaa A. Abdellatef) demonstrated how single cell migration patterns vary as the ECM proteins differ, but there is a lack of research on the effect of the ECM on collective cell migration. Unfortunately, the ECM is disrupted during conventional methods for studying collective cell migration (e.g., scratch wound assays). In this study, a more advanced technique using photoswitchable passivated surfaces was tested and proved to be suitable in observing the cell migration on different ECM proteins. This method achieved region specific ECM adsorption with a significant difference between the specific and nonspecific adsorption. Cells were seeded and attached to the ECM and then were observed as they migrated. The cell migration results suggest that the ECM type is critical to collective cell migration, as the cell clusters exhibit different migration patterns with varying ECM proteins.
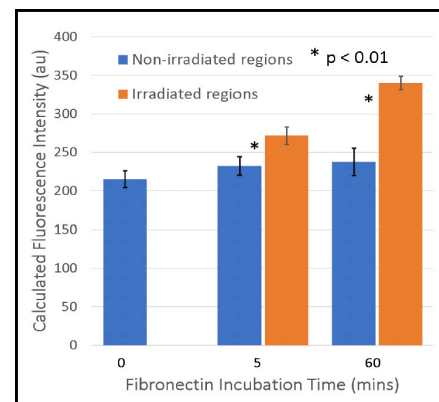
Figure 1: Immunofluorescence results of radiated and nonirradiated regions for samples with different protein incubation times.

Summary of Research:

Photoswitchable passivated glass surfaces have been used to achieve region specific cell adsorption to observe cell migration with no harm to the cells [3]. In this method, the glass has a coating that detaches from the surface upon exposure to ultraviolet (UV) light. Region specific cell adsorption is possible since cells can only attach the irradiated regions. It was hypothesized that this technique could be used to attain region specific ECM adsorption.

Testing Protein Adsorption to Photoswitchable Passivated Glass Surfaces. To take advantage of the photoswitchable passivated glass for this study, the ECM must adsorb onto the glass surface with significant difference between the specific and nonspecific adsorption. To assess the ECM adsorption, the passivated surface was irradiated with circle patterns and exposed to fibronectin for varying incubation times. Ideally, the fibronectin would only adsorb onto the irradiated regions. The samples were then exposed to a primary antibody for fibronectin attached to a fluorophore so the samples could be observed under immunofluorescence.

The immunofluorescence results demonstrated significant difference in calculated fluorescence intensity between the irradiated and non-irradiated regions for both the 5-minute and 60-minute samples (see Figure 1). The irradiated regions of the 60-minute sample also

exhibited a greater calculated fluorescence intensity compared to that of the 5-minute sample. These results prove that fibronectin adsorbs to the surface and that the higher incubation time resulted in a higher density of fibronectin. Since fibronectin was demonstrated to adsorb to the surface with significant difference between specific and non-specific adsorption, this technique using the photoswitchable passivated glass surface was suitable to observe the effect of different ECM proteins on collective cell migration.

Observing Cell Migration. Once the samples had region specific ECM adsorption, cells were cultured onto the samples (see Figure 2). The region outside the cell cluster was then irradiated to remove the coating and more ECM was added. During migration, pictures of the cell clusters were taken every 30 minutes for three
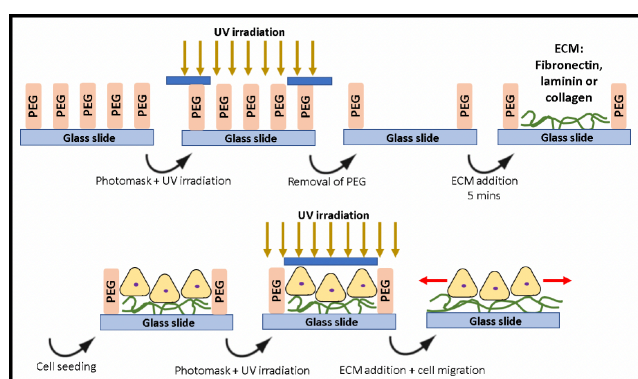

Figure 2: Method using the photoswitchable passivated glass to attain region specific ECM adsorption and observe cell migration.
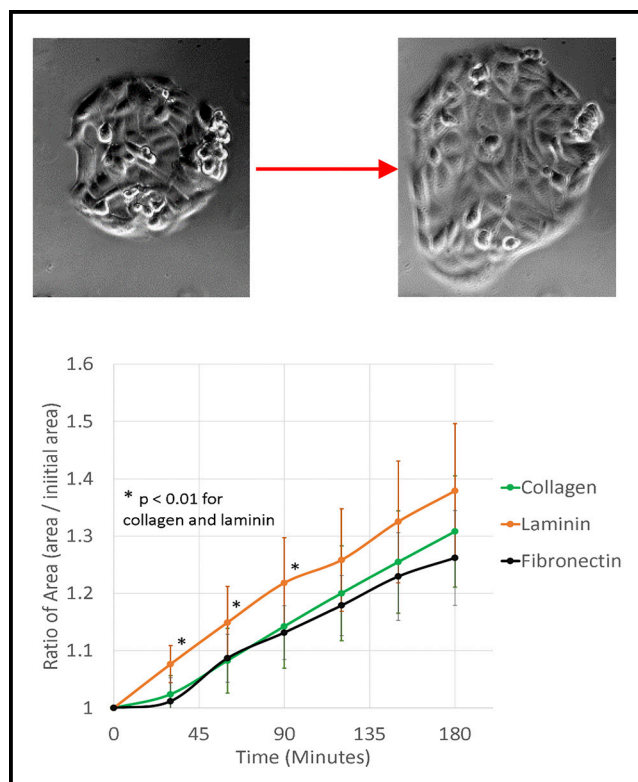

Figure 3: Ratio of area expansion of cell clusters of cells migrating on different ECM proteins with images of the cell cluster on a laminin coated surface at 0 and 180 minutes.

hours. The area of the cell clusters was measured every 30 minutes (see Figure 3).

The cell migration was observed with different ECM proteins: fibronectin, collagen, and laminin. Based on Figure 3, there is a significant difference in area expansion between the cells migrating on collagen coated surfaces compared to that on laminin for the first 90 minutes. This difference in migration suggests that ECM proteins are critical to collective cell migration.

Conclusions and Future Steps:

Understanding how ECM can help or hinder collective cell migration would allow for the manipulation of physiological process such as speeding up wound healing or hindering cancer metastasis. Since conventional techniques for observing collective cell migration disrupt the ECM, a more advanced technique was necessary. This study proved a method using photoswitchable passivated surfaces is suitable to observe collective cell migration on different ECM proteins. Fibronectin, an ECM protein, was demonstrated to adsorb onto the surface in specific patterns with a significant difference between specific and nonspecific adsorption. A greater protein incubation time resulted in a higher density of protein adsorption. After achieving region specific ECM adsorption, cells were seeded and attached to the ECM. The collective cell migration results suggest that the ECM type is critical to migration.

The next steps of this study include confirming that other ECM proteins, like collagen and laminin, also adsorb onto the glass surface through similar immunofluorescence experiments. Further, cell migration patterns are significantly influenced by the cell culturing (i.e., density) before the cells are seeded onto the samples. Therefore, for the fairest comparisons between cell migrations on different ECM proteins, the seeded cells on each sample should come from the same cell cultures. It is important to note that the results in Figure 3 reflect multiple cell migration experiments where the cells were from different cell cultures, which led to large deviation.

Acknowledgments:

References:

[1] Zheng Y, Nan H, Fan Q, Wang X, Liu L, Liu R, Ye F, Sun B, and Jiao Y. Modeling cell migration regulated by cell-ECM micromechanical coupling. Phys. Rev. 2019; 100; 1-11.

[2] Painter K. J. Modelling cell migration strategies in the extracellular matrix. J. Math. Bio. 2009; 58; 511.

[3] Rolli C. G., Nakayama H., Yamaguchi K., Spatz J. P., Kemkemer R., and Nakanishi J. Biomat. 2012; 22; 2409-2418.

Design and Fabrication of a Magnetic Elastomer–Dased Soft Actuator

Rodolfo Cantu

Mechanical Engineering, The University of Texas at Austin

Abstract:

Technological advancements to date have primarily focused on stimulating only two of the five human senses: sight and hearing. Touch-based interactive technologies are still in their infancy. Haptic devices allow tactile interactions between humans and digital interfaces, assisting humans in industries such as healthcare, automotive and entertainment. Magnetorheological elastomers (MREs) based on nanoparticles constitute a promising candidate material for creating tactile interfaces [1] capable of creating high-resolution features on the micron scale [2]. These magneto-responsive elastomers must be integrated with magnetic micro-controls to create the local magnetic fields necessary to actuate deformations.

Summary of Research:

The future of touch-based haptic interfaces relies on the actuation of microscale thin films. Magnetoresponsive soft-actuators have the potential to create low-power, high-responsivity, and low-cost haptic interfaces. A process was developed to create a system of micromagnetic controls integrated into microscale beams made of an MRE. This project is structured into three main objectives: the fabrication and characterization of magnetic microcontrols, the fabrication of a micrometer thin MRE, and the integration of actuation controls and MRE.

Figure 1: Device design of magnetorheological elastomer with two integrated magnetic micro controls.

The design concept involves two micromagnetic controls on the surface of an MRE thin film (see Figure 1). The MRE is constituted of a soft silicone rubber matrix and magnetic nanoparticles forming vertical chains in the thickness direction of the film. The micro controls are made of pillars with circular and elliptical base. The circular magnets (perpendicular magnetic anisotropy (PMA) magnets) are fabricated so that the magnetic moment lies preferentially in the direction perpendicular to their surface. The elliptical magnets (in-plane magnetic anisotropy (IMA) magnets) are deposited to be magnetized in the direction of the long axis. When the controls are embedded into the MRE, their magnetic fields will couple and interact with the elastomer in proximity of the gap between them, causing it to deflect.

The first step in the creation of this device is the fabrication of the magnets. Starting with a 4-inch clean wafer, 350 nm of LOR3A and 450 nm of S1805 (positive) resist were spin coated, following with a soft bake at 180°C for five minutes for the former and at 115°C for one minute for the latter. The coated wafer was then exposed in an ABM contact aligner for 1.5 seconds and developed for 60 seconds using 726 MIF solvent. The patterned wafer was then descummed with oxygen
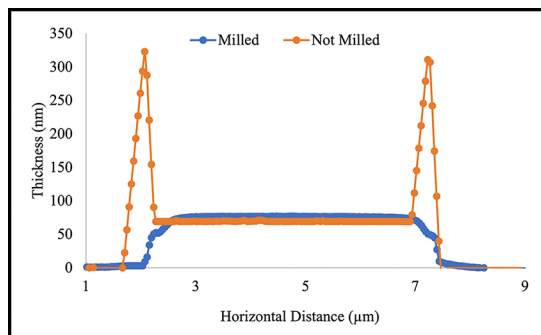
Figure 2: Ion milling to remove "rabbit ears" resulting from sputtering and lift-off.

Figure 4: Magnetic hysteresis loops for short and long axis of IMA ellipses.

plasma for 60 seconds with oxygen flow of 30 sccm and 50 W of power. Then the magnets were deposited via sputtering.

The elliptical pillars were constituted of 3 nm of Ta, 5 nm of Pt, 58 nm of Co, and 5 nm of Pt. The circular pillars were sputtered with 19 alternating layers of Co (1 nm) and Pt (2 nm) and a final 1 nm layer of Co, using the same Ta/Pt underlayer and Pt capping layer as for the elliptical magnets. After sputtering, the wafer was soft baked at 115°C to facilitate the lift-off process, which was performed by first hitting the wafer with pressurized solvents at 1600 psi (C&D SmartProP9000), and submerging it in Remover 1165 for 20 minutes. Finally, an AJA milling tool was used at 600 V for 120 seconds with a 5° tilt to eliminate the "rabbit ears" caused by sputtering and lift-off (see Figure 2).

At this stage, the wafer was diced into 10 × 10 mm devices, each presenting specific geometry and dimensions. The magnetic properties of the deposited magnets were studied via vibrating sample magnetometry (VSM) and the optimal dimensions for both geometries were identified. The hysteresis loops obtained with VSM illustrate the magnetic properties of a magnetic sample, allowing to extract coercivity and remanent magnetization values. The circular pillars, with diameters ranging from 3 to 100 μm were tested for their magnetization in response to an out-of-plane applied magnetic field (see the hysteresis loops in Figure3).
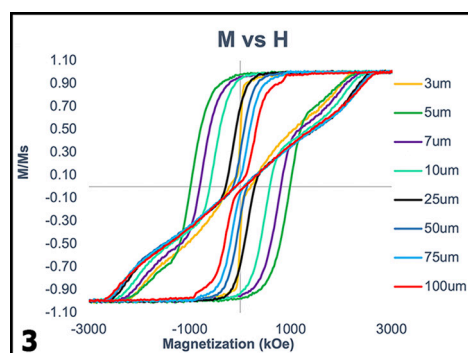
The elliptical samples with in-plane magnetization were measured along both the short and long axes, as shown in Figure 4. The optimal magnetic properties were found in the 5 μm diameter circular magnet (maximum remanent magnetization and coercivity) and the 3 μm (short axis), 15 μm (long axis) elliptical magnet (largest difference between hysteresis loop measured along the two axes). Atomic force microscopy (AFM) was used to confirm the dimensions of the deposited geometries.

Finally, a system of micromagnets (one IMA and PMA magnet spaced apart 1, 1.5, and 2 μm) was ultimately designed to be integrated into cantilevers and simply supported beams made of a micrometer-thin MREs to create a magnetic soft actuator. the elastomer was composed of 95 wt% Sylgard 527 and 5 wt% Sylgard 184. After mixing the two elastomers using a vortex for a few seconds, 6 vol% of Fe nanoparticles were added and mixed for about three minutes. The dispersion was homogenized for 1 hour and 15 minutes using an ultrasonicating bath. Finally, the mix was spin coated on a wafer at 7500 rpm for 60s to achieve a thickness of 2-2.5 μm.

Conclusions and Future Steps:

We demonstrated the fabrication process of micro-magnets and discussed their optimal dimensions to achieve desired magnetic properties. Magnetic simulations carried out in our lab guided the choice of a reasonable spacing between the IMA and PMA magnets when integrated into the soft actuator. Next, the developed controls will need to be embedded into cantilevers and beams with the actuation performance assessed. We believe these results serve as a foundation for the fabrication of soft magnetorheological elastomers with integrated magnetic controls.

References:

[1]   Böse, H., et al. Magnetorheological Elastomers - An Underestimated Class of Soft Actuator Materials. Journal of Intelligent Material Systems and Structures (2021).

[2]   L. Cestarollo, et al. Nanoparticle-based magnetorheological elastomers with enhanced mechanical deflection for haptic displays, ACS Applied Materials and = Interfaces 14 (2022),

Figure 3: Magnetic hysteresis loops for PMA circles.

The Role of Pyridine in the Electrochemical Reduction of CO_2

Dr. Zizwe Chase

Electrical and Computer Engineering, University of Illinois at Chicago

Abstract:

Rising carbon dioxide (CO_2) emissions are a major factor in the rise of the global temperature leading to issues associated with climate change. Capturing and converting CO_2 to useful chemicals that can be used for energy or industrial needs can help allay global warming whilst creating new, sustainable economic development. Electrochemical reactions (ECRs) with platinum (Pt) electrodes have been extensively studied for CO_2 reduction and have shown to heavily favor the hydrogen reduction reaction (HER). There has been a dispute as to whether the addition of pyridine enhanced the production of organic compounds such as methanol and formic acid. Through the *in-situ* use of Sum Frequency Generation spectroscopy (SFGs), a surface sensitive technique, during the ECR of CO_2, we have shown that intermediates and products for organic product formation do not appear at the reaction interface. It also shows that pyridine most likely lays flat on the catalytic surface possibly blocking CO_2 adsorption sites.

Summary of Research:

CO_2 adsorbed on the Pt surface as CO_{ads} has been a known poison hindering its electrochemical reduction to organic products [1]. The addition of pyridine to this system was thought to enhance organic product formation [2] even though conflicting studies have shown the hydrogen reduction reaction (HER) was favored [3]. The question remained as to what chemical species were present at the catalytic interface.

Sum Frequency Generation spectroscopy (SFGs) was used as a tool for *in-situ* investigation of the species at the interface. SFG is powerful in that it only detects species at a non-centrosymmetric interface via the use of two spatially and temporally overlapped lasers. There are no contributions from any species in bulk solution to the detected signal. The electrochemical cell used for the *in-situ* study was filled with 0.1M $NaClO_4$ solutions. This solution either contained 0.01M pyridine or it did not, and both were in the presence of CO_2. The working electrode was a Pt disk, the counter-electrode was Pt, the reference electrode was Ag/AgCl (NaCl saturated), the optical window used was made of CaF_2, and the SFG was measured in the ppp polarization combination. Complimentary cyclic voltametric (CV) studies were done for each system.

SFG was conducted first on the solution that had no pyridine with the electrode saturated with CO_{ads}. Figure 1 shows that as the overpotential is lowered from -400mV to -1000mV there is a red shift of the CO_L peaks, which is as expected from previous works [4-6]. The peaks were fit to a Lorentzian lineshape to elucidate the characteristic spectral features. The resulting Stark shift from this system (from the decreasing peak center with potential) was higher than reported number most likely due to a differing cationic structure at the interface in the presence of the applied field. The frequency shift is also characteristic of either dipole-dipole coupling or an increase in the back-donation of electrons from the Pt surface to the CO π^* antibonding orbitals [7]. A decrease in the peak amplitude with lowering potential could be indicative of a less upright COL configuration while an abrupt change in the FWHM at -1000mV could be adlayer reordering [.8]

Next the system with pyridine was studied. CV showed the CO_{ads} was irreversibly adsorbed and a pyridine species reduced at -600mV. SFG showed that CO_L does not shift, loses intensity, and is disappears from -700mV onwards (Figure 2, Top). This could be a possible coverage loss, re-orientation, or disordering of adsorbed species. Also noticed was the presence of the C=C aromatic stretch (Figure 2, Bottom), which had potential independent intensity and linewidth shape. No species were noticed for formic acid or the formate anion, which are the thermodynamically favored species. The pyridine is possibly undergoing no molecular re-orientation and could be possible flat on the surface. Measurements in ppp are sensitive to the molecular average tilt [5].

Conclusions and Future Steps:

The addition of pyridine to the system on Pt electrodes might be in fact blocking CO_2 adsorption sites leading to higher rates of HER versus organic product formation as reported in literature [3] as the pyridine may be laying flat on the Pt surface. No organic products were seen. CO_{ads} is probably disordered at the surface possibly decreasing the kinetic rate towards organics. In order to further prove that there are no organic species at the interface we would like to probe from 1200-1500 cm^{-1} to see if any acetate species form.

Acknowledgements:

References:

[1]   Hori, Y., Electrochemical CO_2 Reduction on Metal Electrodes, in Modern Aspects of Electrochemistry, C.G. Vayenas, R.E. White, and M.E. Gamboa-Aldeco, Editors. 2008, p. 89-189.

[2]   Barton Cole, E., et al., Journal of the American Chemical Society, 2010.

[3]   Chen, X.-J., et al., ACS Catalysis, 2021.

[4]   Humbert, C., et al., The Journal of Physical Chemistry C, 2016.

[5]   Lu, G.Q., et al., Surface Science, 2005.

[6]   Yang, S., et al., Electrochimica Acta, 2017.

[7]   Tadjeddine, A. and A. Peremans, Surface Science, 1996.

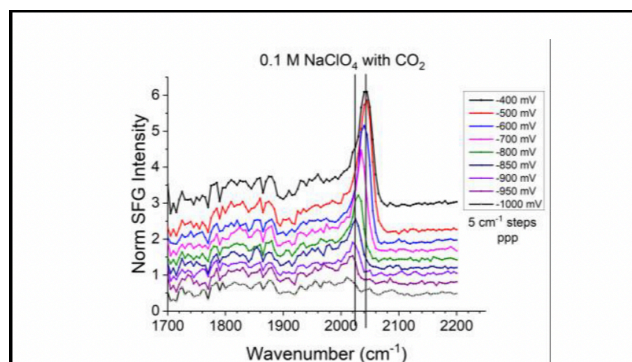[8]   Wallentine, S., et al., The Journal of Physical Chemistry A, 2020.

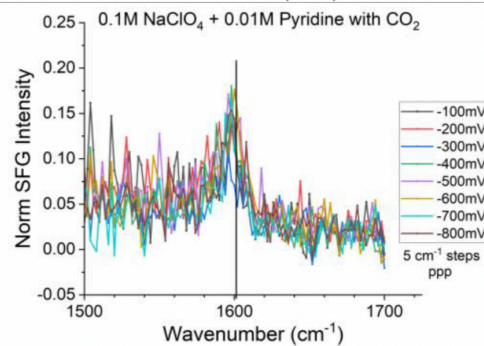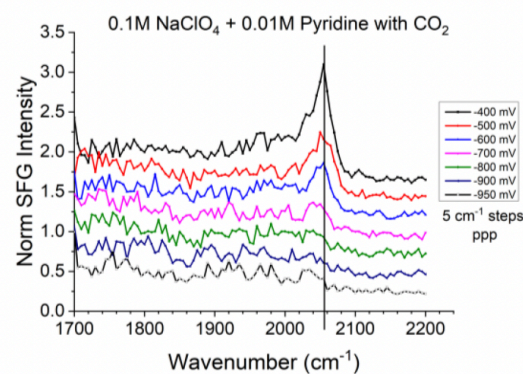Figure 1: The potential dependent SFG spectra of 0.1 M $NaClO_4$ with CO_2.

Figure 2: The potential dependent SFG spectra of 0.1 M $NaClO_4$ and 0.01M pyridine with CO_2.

Observing Receptor Layer Swelling on Piezoresistive Devices

DeShea Chasko

BioMedical Engineering, Mississippi State University

Abstract:

A surface stress sensor converts forces that are applied to its surface into a measurable, electrical signal. Polymers have been deposited onto a Membrane-Type Surface stress Sensor (MSS) chip as a receptor layer of target molecules. Under gaseous conditions, the polymer layer swells, which directly affects the sensitivity of the sensor. An improved understanding of how to recreate the swelling on a flat silicon surface and MSS chip will be instrumental in optimizing the sensitivity of the MSS chip, creating a further step towards personalized medicine and efficient agricultural techniques.

Summary of Research:

Cantilever surface stress sensors are commonly used, especially in biological and chemical applications [1]. Different polymer layers can be coated on a cantilever beam which can directly affect what is detected [1]. The deflection of the cantilever can be measured optically, using a laser, or electronically, using a piezoresistor. When a stress is applied to the surface of the sensor, a piezoresistor can measure changes in electrical resistance. The sensitivity of the piezoresistor is heavily influenced by its location on the cantilever and the overall sensor geometry. To improve the sensitivity and reliability of the piezoresistor reading, an MSS chip was designed and created [2].

The MSS chip contains an adsorbate membrane that is suspended by four piezoresistive beams [2]. There are two different piezoresistive designs on the chip in order to ensure an optimal reading. The membrane is clamped down on the four beams which enables deflection to be measured in four directions, this can be seen in Figure 1 [1].

Since the piezoresistive bridges are all clamped, the beams can measure accurate profile of the applied surface stress [2]. The MSS chip works by absorbing surrounding gasses and then produces an electrical signal that can be evaluated [2]. As a result, prior experimentation found that an MSS chip is up to 100

F. Loizeau, T. Akiyama, S. Gautsch, P. Vettiger, G. Yoshikawa, and N. De Rooij, "Membrane-Type Surface Stress Sensor with Piezoresistive Readout," *Procedia Eng.*, vol. 47, pp. 1085–1088, Jan. 2012.
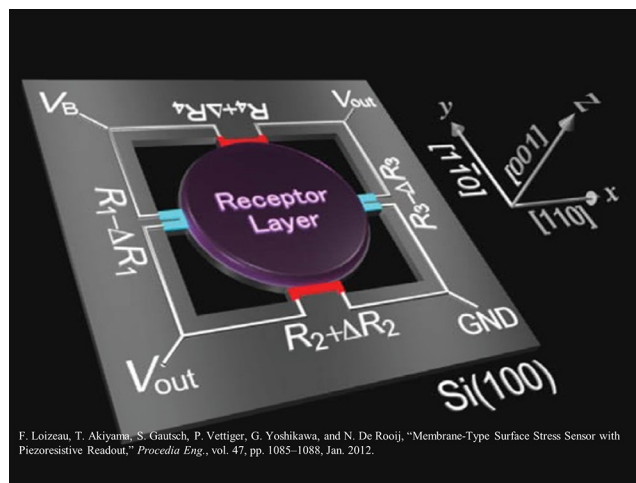
Figure 1: A schematic of the MSS chip [1].

times more sensitive than a conventional piezoresistive cantilever beam [3]. Different polymers can be deposited onto the suspended membrane using inkjet spotting which can then be tailored for use in detecting desired substances.
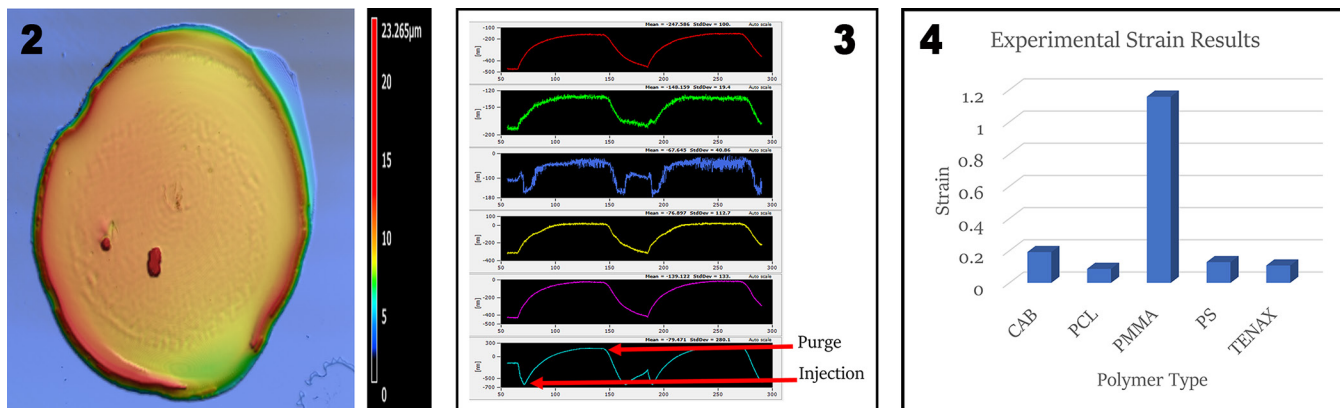
Figure 2, left: A smooth, round polymer (PMMA) deposited on a silicon surface. Figure 3, middle: Phase monitor graph depicting gas injection and purging. Figure 4, right: Experimental polymer strain values when exposed to water.

Since the piezoresistor measures induced surface stresses, changes in the surface characteristics of the polymer affect the chips sensitivity. It is still unknown how different polymers react when in contact with different gasses. This project focused on creating an experimental setup to better understand the gas-polymer swelling relationship.

Conclusions and Future Steps:

The first focus of this project was to utilize an inkjet spotter to create round, flat polymer droplets. The inkjet spotter deposits polymer solutions at different rates and sizes. An optimal recipe was created that deposited 400 shots of polymer onto a desired surface. An example of the deposited polymer shape is shown in Figure 2.

The next focus was to monitor the polymer swelling under different gaseous conditions. Polymer swelling is difficult to see with the human eye, but there are tools and techniques to observe surface changes in real time at the nanoscale level. The tool used for these experiments is the Digital Holographic Microscope (DHM). This technology allows for real time monitoring of the polymer swelling process. Therefore, it is easy to track and record the exact moment when gas is being injected into and purged from the polymer layer. A LabVIEW program was created that cyclically introduced gas into the system every other two minutes and ran for eight minutes total. Once all of the images were recorded for each experiment, the surface profiles of the polymer layers were analyzed using a laser microscope. Figure 3 illustrates the moments when gas was injected into and purged from the system.

The final focus was to compare the surface characteristics of the polymer under normal conditions and when swelled. This comparison allowed for the calculations of the strain of each polymer experienced under specific gaseous conditions. Strain was calculated by subtracting the deformation recorded by the phase monitor from the initial average surface height of the polymer divided by the initial average surface height. By calculating the strain, insight can be gained into ensuring the right polymer is coming into contact with target gasses for their desired application. Examples of polymer-gas strain calculations are shown in Figure 4.

In the future, a variety of polymer-gas interactions will be recorded and analyzed using this experimental setup to build a library of these relationships. Isolating polymers according to their ideal strain characteristics using a certain gas will be crucial for controlling the swelling effects on MSS piezoresistors. Different inkjet recipes will also be used to create different polymer shapes and sizes. Additionally, efforts will be made to better understand the root causes and effects of polymer swelling. Modeling the polymer-gas swelling relationship is the ideal way to determine which gas should be introduced to which polymer. Building the library of these interactions is an instrumental step to most accurately model this phenomenon which will create a step closer towards personalized medicine and agricultural techniques.

References:

[1]   F. Loizeau, T. Akiyama, S. Gautsch, P. Vettiger, G. Yoshikawa, and N. De Rooij, "Membrane-Type Surface Stress Sensor with Piezoresistive Readout," Procedia Eng., vol. 47, pp. 1085-1088, Jan. 2012, doi: 10.1016/J.PROENG.2012.09.339.

[2]   G. Yoshikawa, T. Akiyama, S. Gautsch, P. Vettiger, and H. Rohrer, "Nanomechanical membrane-type surface stress sensor," Nano Lett., vol. 11, no. 3, pp. 1044-1048, Mar. 2011, doi: 10.1021/NL103901A/SUPPL_FILE/NL103901A_SI_001.PDF.

[3]   G. Yoshikawa, et al., "Two-Dimensional Array of Piezoresistive Nanomechanical Membrane-Type Surface Stress Sensor (MSS) with Improved Sensitivity," Sensors 2012, Vol. 12, 15873-15887, vol. 12, no. 11, pp. 15873-15887, Nov. 2012, doi: 10.3390/S121115873.

Ytterbium–Substituted Clathrate Thermoelectrics: Deflection of Phonons Through 'Rattling'

Adam Eichhorn

Materials Science and Engineering Department, Iowa State University

Abstract:

Clathrate or 'cage and rattler' thermoelectric materials are promising candidates for high-efficiency thermoelectricity, offering low thermal conductivities. Barium germanide clathrates have been synthesized in previous studies with moderate efficiencies. Six bulk samples of barium germanide were synthesized, substituting small amounts of ytterbium into the barium stoichiometry. Upon x-ray diffraction (XRD), energy dispersive spectroscopy (EDS), and thermoelectric analysis, the ytterbium substitution was unsuccessful in increasing thermoelectric properties. The presence of secondary phases that sequestered ytterbium prevented the substitution of the Yb ions into the Ba clathrate sites.

Summary of Research:

The stoichiometry of the germanide clathrate samples is $Ba_{8-x}Yb_xGa_{16}Ge_{30}$, where x is 0, 0.2, 0.4, 0.6, 0.8, and 1.0 in samples 1-6, respectively. The type-I clathrate metal shot was used as the precursor for synthesis, with the barium weighed in a glove box to minimize oxidation. The metal was combined and melted in an arc furnace, forming ingots around 6 g in mass. The ingots were broken and pulverized in a ball mill, then the powder was sieved down to 52 μm and 2 g was packed into a die for spark plasma sintering (SPS). The SPS sintered at 840°C and 30 MPa for 30 min. After bulk synthesis, the samples were polished and sectioned for analysis.

Thermoelectric analysis was performed using a Netzsch LFA Hyperflash and an Ulvac-Riko ZEM2. EDS was performed using a scanning electron microscope (SEM).

The data were inconsistent in establishing a trend between Yb content and thermoelectric efficiency, ZT, as shown in Figure 4. Similarly, the lattice thermal conductivity in Figure 3 shows no consistent trend with Yb content. The EDS image in Figure 2 provides an explanation for this inconsistency. The sequestration of Yb in specific regions, likely YbO_2, prevented any Yb from substituting into the Ba sites and consistently changing the structure.

Cubic Pm-3n (Type-I) clathrates
$A_8B^{III}_{16-x}B^{IV}_{30+x}$
A = Sr, Ba, Eu etc.
B^{III} = Al, Ga, In
B^{IV} = Si, Ge, Sn

Figure 1: Barium and ytterbium rattler atoms are held in the alternating tetrakaidecahedron and decahedron cages in the Pm-3n structure, which are made up of the germanium and gallium atoms.

Conclusions and Future Steps:

The mechanism for the decrease in thermal conductivity is inconsistent between samples, due to the formation of ytterbium and ytterbium oxide secondary phases. At low grain size, these phases impede phonon motion, but at large grain size they increase thermal conductivity. Minimal Yb substitution occurred, failing to reproduce the high ZT and solubility limit of 0.7 reported in [11].

Future research can explore the magnetic properties of these samples to identify the valence state of the Yb ions to explain the changes in conductivity. Additionally, samarium germanide clathrates are a similar material with promising clathrate properties.
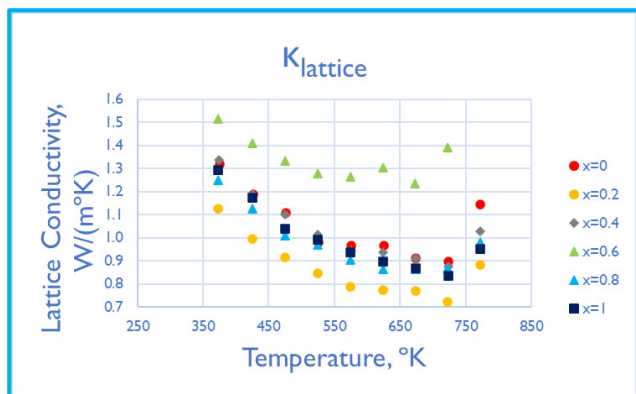

Figure 2: EDS image of the x=0.4 sample, isolating the Yb atomic signal. White regions show significant Yb sequestering and inhomogeneity.
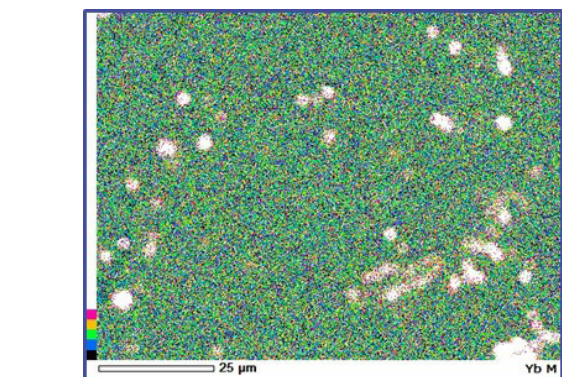

Figure 3: Lattice thermal conductivity of all 6 samples, calculated using the Wiedemann-Franz law to remove the electronic thermal conductivity contribution.
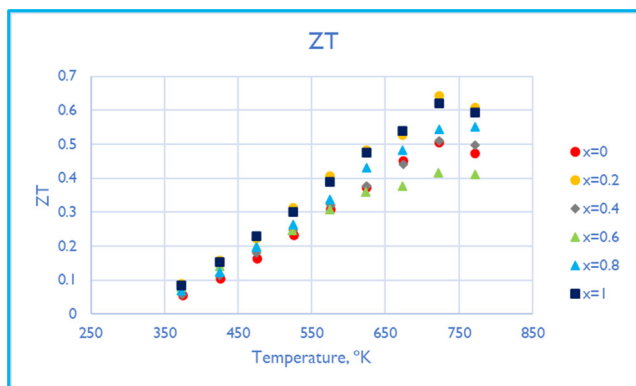

Figure 4: Thermoelectric efficiency of all six samples.

References:

[1] Chen, Y., Du, B., Kajisa, K., and Takabatake, T. (2014). Effects of In Substitution for Ga on the Thermoelectric Properties of Type-VIII Clathrate Ba8Ga16Sn30 Single Crystals. Journal of Electronic Materials, 43(6), 1916-1921. https://doi.org/10.1007/s11664-013-2909-0.

[2] Kawaguchi, T., Tanigaki, K., and Yasukawa, M. (2000). Ferromagnetism in germanium clathrate: Ba8Mn2Ge44. Applied Physics Letters, 77(21), 3438-3440. https://doi.org/10.1063/1.1328048.

[3] Koga, K., Anno, H., Akai, K., Matsuura, M., and Matsubara, K. (2007). First-principles study of electronic structure and thermoelectric properties for guest substituted clathrate compounds Ba6R 2Au6Ge40 (R = Eu or Yb). Materials Transactions, 48(8), 2108-2113. https://doi.org/10.2320/matertrans.E-MRA2007865.

[4] LFA 467 HyperFlash. (n.d.). Retrieved July 31, 2022, from https://analyzing-testing.netzsch.com/en/products/thermal-diffusivity-and-conductivity/lfa-467-hyper-flash-light-flash-apparatus.

[5] Li, Y., and Ross, J. H. (2003). Ferromagnetism in Fe-doped Ba6Ge25 chiral clathrate. Applied Physics Letters, 83(14), 2868-2870. https://doi.org/10.1063/1.1616658.

[6] Liu, L. H., Wei, Y. P., Yang, S. W., Zhu, J., and Li, Y. (2014). Yb-substituted clathrates Ba8-xYbxGa 16Ge30. International Journal of Modern Physics B, 28(23). https://doi.org/10.1142/S0217979214501513.

[7] Liu, L., Li, F., Wei, Y., Chen, N., Bi, S., Qiu, H., Cao, G., and Li, Y. (2014). Synthesis and thermoelectric properties of rare earth Yb-doped Ba 8-xYbxSi30Ga16 clathrates. Journal of Alloys and Compounds, 588, 271-276. https://doi.org/10.1016/j.jallcom.2013.10.219.

[8] Paschen, S., Gspan, C., Grogger, W., Dienstleder, M., Laumann, S., Pongratz, P., Sassik, H., Wernisch, J., and Prokofiev, A. (2008). Investigation of Yb substitution in the clathrate phase Eu8Ga16Ge30. Journal of Crystal Growth, 310(7-9), 1853-1858. https://doi.org/10.1016/j.jcrysgro.2007.11.126.

[9] Ross, J. H., and Li, Y. (2009). Superconductivity and magnetism in silicon and germanium clathrates. In Nanoscale Magnetic Materials and Applications (pp. 105-122). Springer US. https://doi.org/10.1007/978-0-387-85600-1_4.

[10] Shevelkov, A. v. (2008). Chemical aspects of the design of thermoelectric materials. Russian Chemical Reviews, 77(1), 1-19. https://doi.org/10.1070/rc2008v077n01abeh003746.

[11] Tang, X., Li, P., Deng, S., and Zhang, Q. (2008). High temperature thermoelectric transport properties of double-atom-filled clathrate compounds YbxBa8-xGa16Ge30. Journal of Applied Physics, 104(1). https://doi.org/10.1063/1.2951888.

[12] Toberer, E. S., May, A. F., and Snyder, G. J. (2010). Zintl chemistry for designing high efficiency thermoelectric materials. In Chemistry of Materials (Vol. 22, Issue 3, pp. 624-634). https://doi.org/10.1021/cm901956r.

[13] Zhu, X., Chen, N., Liu, L., and Li, Y. (2012). Study on rare-earth-doped type-I germanium clathrates. Journal of Applied Physics, 111(7). https://doi.org/10.1063/1.3671396.

Development of Functional Gas Diffusion Layers for use in CO$_2$ Reduction Reactors via Microscale Printing

Zeinab Ismail

Physics, St. John's University

Abstract:

In a world reliant on the burning of fossil fuels to run some of its major industries, there is concern as to how we dispose of the carbon dioxide (CO$_2$) waste produced. One approach is to reprocess the CO$_2$ into simple hydrocarbons using a CO$_2$ Reduction Reactor (CO$_2$RR). A CO$_2$RR's ability to produce useful products relies heavily on its gas diffusion electrodes (GDEs), which consist of porous membranes called gas diffusion layers (GDLs) coated in a metal catalyst. GDLs act as a barrier against unwanted liquids, letting only gasses pass through.

A conventional GDE, consisting of PTFE and copper covered carbon paper, typically operates for a few hours before its efficiency begins to drop and it floods. Printing GDLs using a 3D printer would allow for optimization of the layer through the customization of the pore size, structure, and density of the layer.

Summary of Research:

The CO$_2$RR used consisted of three SLA-printed compartments: gas, anolyte, and catholyte compartments. The anode, ion-exchange membrane, and cathode used in the reactor were respectively a platinum mesh, nafion ion exchange membrane, and 3D printed GDL created using the NanoScribe GT2, attached to an adapter made by the Objet 30 printer, and sputtered in copper. The reactor was constantly being pumped with carbon dioxide gas and electrolytic solution, consisting of water and potassium bicarbonate. The process of creating functional GDLs was broken into three parts: designing a GDL, creating the gas diffusion electrode, and assembling the reactor and testing it.

The NanoScribe GT2 sweeps a femtosecond near IR laser across resin, curing sections with two-photon polymerization. The two resins experimented with to produce the GDLs were the IP-S and IP-Q resins. The general workflow for the NanoScribe consisted of creating a CAD model and generating an STL, slicing the STL using DeScribe, prepping the resist on a silicon wafer, loading the wafer into the printer, and printing, unloading, and developing the sample. The first design

attempt to generate the full-scale layer of 10.095 mm × 10.095 mm × 400 μm thickness was too computationally intensive. The NanoScribe slicer, DeScribe, can work with files up to two gigabytes, but the full-scale GDL, in its lowest quality, was six gigabytes.

The next design created an STL out of 1/16 of the full-scale layer, one block, and used a for-loop of arrays and an overlap of 5 μm to build the full layer. The layer printed using this design began to deteriorate and peel off the silicon wafer after development. The final GDL design made and used was a 2 × 2 array of 5 mm × 5 mm × 100 μm each block, layered on top of each other four times, to create a thickness of 400 μm.

Using the IP-S resin and 2 × 2 array design, a second GDL print was made. After development, the GDL layers began to fall apart, and the layer began to peel off the wafer. At this point, the suitability of the IP-S resin was put in question.

The IP-S resin was initially chosen because it was not sensitive to overdevelopment and was the freshest resin available. It was only after printing the third gas diffusion

using IP-Q resin instead that the layer turned out better than previous prints, with the IP-Q resin layer having no visible discoloration, excess uncured resin, or separation of layers from each other or off the wafer (see Figure 1).

After developing the layer in PGMEA for 45 minutes and IPA for 30 min, it was soaked for another 30 minutes in IPA. Next, it was sonicated for 10 minutes at 21°C, then placed on a hot plate of 90°C for 20 seconds and moved onto a cool plate. After doing this twice, the layer popped off the wafer.

Then the layer was glued to an adapter printed on the Objet 30 and cured using UV light. Afterwards, the glued pieces were sputtered with a 254 nm layer of copper, using the AJA sputter machine (see Figure 2). Finally, the CO_2RR was assembled, and the finished gas diffusion electrode was incorporated into it (see Figure 3).

The CO_2RR was connected to a power source, potentiostat, and peristaltic pump. However, the gas chromatograph, a machine that would collect and quantify the gas products, was not working. The IR drop was collected and was found to be similar to an IR drop of a conventional GDL on the market. Then a cyclic voltammetry (CV) scan, which measures the change in current as different potentials are applied, was generated. Ideally, the plot should have multiple peaks, each peak representing the reduction/oxidation process. However, as shown in Figure 4, there's no current in the cell until about -1.2 V of potential is applied. This conclusion informs us that there is an electrochemical reaction taking place. However, there is another issue preventing a proper CV scan from being generated.

When the GDL was taken out of the cell, it was discovered that the copper wasn't adhering well to the GDL. A possible solution to try down the line would be to coat the layer initially with another metal, like chromium, then coat it with copper.

Conclusion and Future Steps:

Through the lengthy process of designing the gas diffusion layer, 3D printing it, and running it in a CO_2RR, we were able to produce a GDL that has a similar IR Drop to a conventional market GDL. More importantly, the GDL did not flood during the process of running the cell, showing the potential of using microscale manufacturing in producing optimized GDLs. The next steps would be to try coating the printed GDLs with a hydrophobic coating, as well sputtering it with chromium and copper. Afterwards, it would be tested in the CO_2RR when the gas chromatograph is working.

References:

[1] Energy Environ. Sci., 2021, 14, 3064.

[2] Wakerley, D., Lamaison, S., Wicks, J. et al. Gas diffusion electrodes, reactor designs and key metrics of low-temperature CO_2 electrolysers. Nat Energy 7, 130-143 (2022). https://doi.org/10.1038/s41560-021-00973-9.

Figure 1, top: IP-Q resin layer with no visible discoloration, excess uncured resin, or separation of layers from each other or off the wafer.

Figure 2, second from top: A 254 nm layer of copper was added using AJA sputter deposition.

Figure 3, third from top: Assembled CO_2RR with gas diffusion electrode incorporated.

Figure 4, bottom: Electrochemical reaction.
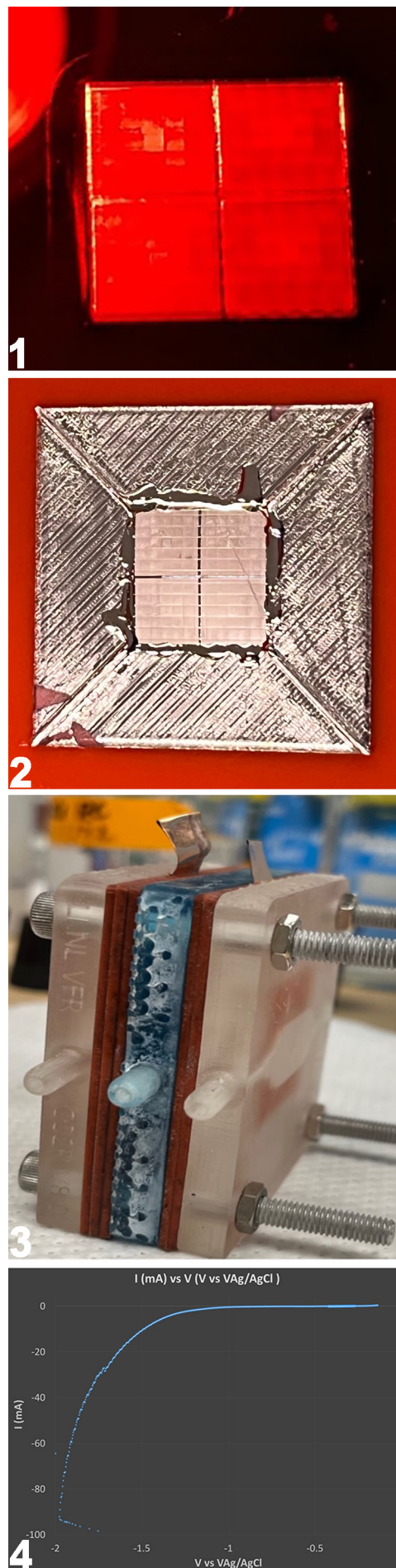
Decoherence Phenomena in Nitrogen-Vacancy Diamond

Aulden Keating Jones

Physics, Georgia Institute of Technology

Abstract:

Nitrogen vacancy (NV) centers in diamonds are atom-sized spin defects whose unique properties enable their use as robust quantum sensors. Recent research efforts have focused on NV magnetometry, where both single and ensemble NVs are used for highly sensitive magnetic field detection with nanoscale spatial resolution. While NV sensors have been successfully applied to many fields, ensemble NV diamonds are still below the sensitivity threshold needed for many more potential applications. This project aims to investigate the relationship between crystallographic strain and the spin coherence time T_2^* in NV-diamonds grown by chemical vapor deposition (CVD). A better understanding of this relationship can provide valuable input for improving diamond growth methods and eventually extending T_2^*.

Summary of Research:

While CVD allows for relatively high control over the depths and concentrations of nitrogen impurities, samples produced this way can contain unwanted and sometimes large strain features. This crystallographic strain can couple to NV spins, resulting in faster dephasing and lower DC magnetic field sensitivity.

Although it is understood that this stress decreases NV coherence, the exact details of the interaction are relatively unknown. For example, there still exists uncertainty in widely used spin-strain coupling coefficients in addition to the effects that large (sample-sized) strain patterns have in high-stressed crystals [2].

Dephasing Mechanisms. T_2^* is a decay constant that characterizes the coherence time of our NV spins. When static or gradually changing inhomogeneities are present within a sample, T_2^* will be shortened, resulting in decreased magnetic field sensitivity. Common contributors to dephasing are shown in the equation displayed in Figure 1.

Samples. Both high and low strain samples were used, allowing observation of strain effects in different diamond environments. The nitrogen limited T_2^* value was 1.6 μs for the lower strain sample (Figure 4) and 2.5 μs for the higher strain sample (Figure 2). This means that our measured T_2^* can only take values between the limited maximum and zero.

$$\overline{T_2^*} \approx \overline{T_2^* \{\text{electronic spin bath}\}} + \overline{T_2^* \{\text{nuclear spin bath}\}}$$
$$+ \frac{1}{T_2^* \{\text{strain gradients}\}} + \frac{1}{T_2^* \{\text{electric field noise}\}}$$
$$+ \frac{1}{T_2^* \{\text{magnetic field gradients}\}} + \frac{1}{T_2^* \{\text{temperature variation}\}}$$
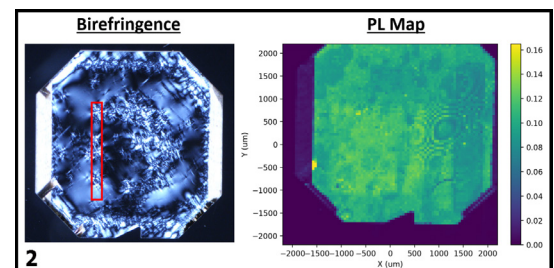$$+ \frac{1}{T_2^* \{\text{unknown}\}} + \frac{1}{2T_1}, \quad (18)$$

Figure 1, top: Equation for T_2^* in terms of common contributors to spin dephasing [1]. Figure 2, bottom: Birefringence image and photoluminescence colormap of the higher strain sample. The red outline shows the location of the line test in Figure 3.
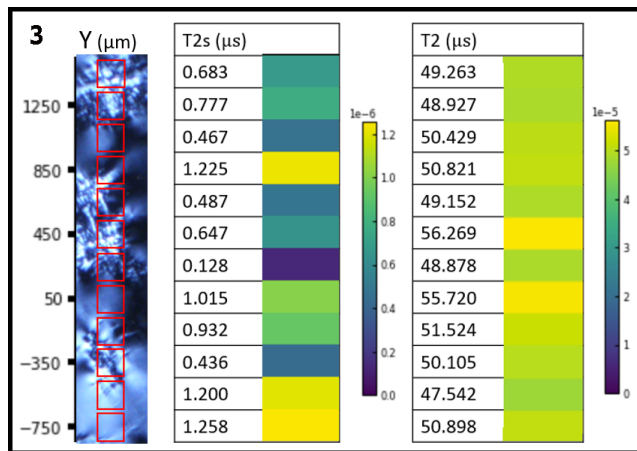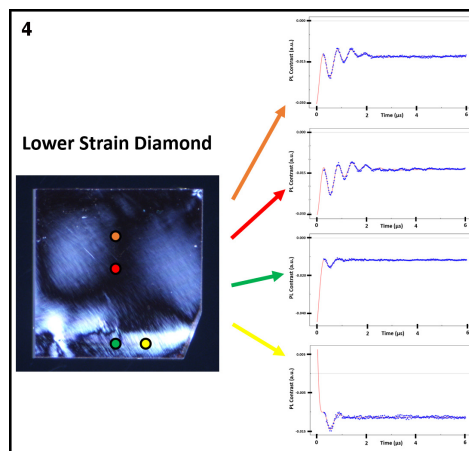
Figure 3, left: T*2 and T*2 values for a single line test in the high strain sample. Figure 4, right: Comparison of free induction decay (FID) curves at different strain locations. T*2 shown to decrease in areas of high strain.

Measurement Technique. To study the correspondence between strain and T^*_2 both birefringence microscopy and optically detected magnetic resonance (ODMR) techniques were used. The Deep Focal Depth Confocal (DFDC) microscope, an instrument designed and built by Dr. Masuyama, was used to measure T^*_2. The primary components consist of a 532 nm green laser for optical initialization and readout, a coplanar waveguide to supply uniform microwave control pulses, and a permanent magnet to lift spin-state degeneracies. A movable stage was used to control the position of samples with respect to the beam. Traditional birefringence imaging was used to determine the strain features present within each sample. This was then overlaid with a photoluminescence (PL) map taken by continuously scanning the laser over the sample's surface. Both images for the higher strain sample are shown in Figure 2. After several calibrating pulse measurements, a Ramsey sequence was performed to determine T^*_2 at each location tested. The sequence consists of a microwave π/2 pulse, followed by a variable interval of free precession, and ended by a second π/2 pulse. The result of repeating this sequence over increasing intervals of free precession is a free induction decay curve, whose exponential decay constant gives the value for T^*_2.

Results. Initial tests on the lower strain diamond confirmed the assumption that strain results in lower T^*_2 values (Figure 3). Further tests on the high strain diamond also show a correspondence between dislocation bundles and the lowest T^*_2 measurements (Figure 4). T^*_2 values were also measured at these locations to rule out the possibility of nitrogen concentration discrepancies causing the dephasing differences. Whether or not this trend is a direct result of crystal strain remains to be fully understood. There are many points where the relative strain seen in the birefringence image and the measured T^*_2 value do not follow the expected relationship of higher observed strain leading to lower coherence times. Such as at the 450 and 250 µm positions. It should be noted that the current experimental setup is only sensitive to crystallographic strain along the NV axis the laser is

aligned with. Therefore, there are components of the stress tensor we are insensitive to and thus features in the birefringence image that we do not sense the effects of.

Conclusion and Next Steps:

These results are the first attempt at mapping and characterizing the strain-T^*_2 relationship in these diamond samples on a newly designed instrument. Future efforts will be to refine the experimental and data analysis techniques used to obtain T^*_2 values in addition to testing more samples. An important observation is that the maximum T^*_2 values observed in even the most uniform areas displayed values that were each around half of their nitrogen-limited maximum. This suggests that there is an unaccounted-for dephasing mechanism or non-optimized instrumentation parameters preventing these maximum values. Inhomogeneous magnetic fields, electric fields, or temperature gradients could all play a part, and limiting or accounting for their effects must be done to fully characterize the effect that crystallographic strain may have on our samples.

Acknowledgements:

References:

[1] J. F. Barry, J. M. Schloss, E. Bauch, M. J. Turner, C. A. Hart, L. M. Pham, and R. L. Walsworth, Rev. Mod. Phys. 92, 015004 (2020).

[2] P. Kehayias, M. J. Turner, R. Trubko, J. M. Schloss, C. A. Hart, M. Wesson, D. R. Glenn, and R. L. Walsworth, Physical Review B 100, 174103 (2019).

Microfluidic Handling of DNA for Spatial Genome Research

Eryka Kairo

Physics Department, Seton Hall University

Abstract:

Nuclear envelope invaginations that contain endoplasmic reticulum (ER), mitochondria and other cytosolic organelles have been linked to cancer, and can be used as tumor biomarkers. To gain a better understanding of how this occurs, the organization and composition of chromatin near nuclear invaginations needs to be examined. Assuming that these invaginations are involved in cell signaling and transcription, they may control disease-specific phenotypes through spatial gene regulation. To explore spatial control of gene regulation, we have developed a method that enables chromatin isolation from small (femtoliter scale) targeted volumes within the nucleus. The method, we call Femto-seq, uses localized nonlinear excitation to photo-biotinylate small nuclear volumes so that chromatin can be obtained using affinity purification, and then sequenced. To improve the throughput and efficacy of Femto-seq, here we demonstrate a microfluidic purification device utilizing a single fluidic channel with a functionalized surface and mixing elements that improve sample yield and the level of purification. When validated and employed, our microfluidic devices will enhance the capacity of Femto-seq to elucidate spatial gene regulation patterns associated with nuclear invaginations. The device was fabricated using multilayer SU-8 photolithography. Herringbone structures were added along the fluidic channel to encourage "chaos" in flow patterns of our sample through the channel, increasing the capture efficiency and improve our purification yield. We utilized a negative resist and our design was cast into PDMS and bonded to a glass surface. Our device was characterized through fluorescence microscopy and biochemical assays to first, validate that a streptavidin-biotin complex is formed using a glass functionalization protocol, and then to optimize an elution protocol suitable for our device and quantify our yield and purity of biotinylated deoxyribonucleic acid (DNA).

Summary of Research:

Our project goal for this summer was to fabricate and optimize a microfluidic device that can immobilize biotinylated DNA. The device design was already determined by mentor Jack Crowley, which was a single fluidic channel that had added mixing elements called herringbones on the top of the channel, both embedded in a layer of polydimethylsiloxane (PDMS) as shown in Figure 1.

The PDMS is then binded onto a glass slide to close the channel. To achieve this goal, the project had three main parts. The first part was the wafer fabrication and the device construction, and our methodology for this part was to use multi-layer SU-8 soft photolithography
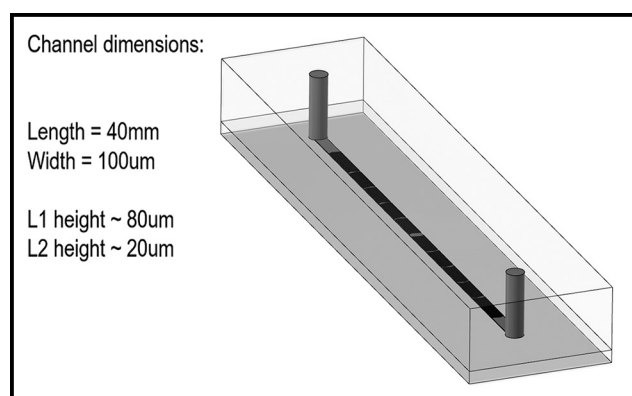
Channel dimensions:

Length = 40mm
Width = 100um

L1 height ~ 80um
L2 height ~ 20um

Figure 1: Schematic design of microfluidic device.

because the design required the fluidic channel to be treated as one layer during photolithography, and the herringbones to be treated as another; the second part was to functionalize the device surface in order to immobilize streptavidin on to the glass substrate and take advantage of the very strong affinity between streptavidin and biotin; the final part was validation and characterization of the device, and to set up an engineering system to optimally operate the device.

The first portion of the project took the longest because we were in unfamiliar territory working with multi-layer photolithography — so there was a lot of trial and error. Issues arose when we weren't able to achieve proper contact between our silicon wafer and our photomasks, but by talking to Aaron Windsor and Chris Alpha from the CNF staff, we were able to gather some tips and tweak our fabrication process, which yielded better results.

Upon being able to consistently acquire usable channels from this process we were able to move on to the functionalizing portion of the project. This portion involved functionalizing fully constructed devices and validating the protocol worked as intended.

To do this we used fluorescent microscopy and flowed fluorescent biotin through functionalized devices, to image and search for bright sports which correlate to immobilzed biotin. We were able to see that we were immobilizing some biotin, so the next step was to set up an experiment to characterize our device. We chose to use DNA gel electrophoresis to do this as we are able to quantify the DNA bands in the agarose gel after the process, so we would be able to get quantitive data.

We set up the experiment by using DNA gel extraction on a DNA ladder to biotinylate a single length of DNA, and then flowing the ladder and the biotinylated DNA through our device and collecting the flow through. The flow through was run through the gel alongside some baseline samples to learn as much as we could about our device.

Conclusions and Final Steps:

Our next steps begin with completing an engineering system to operate the microfluidic chip. This includes setting up a system that adds an oscillatory washing step within the fluidic channel to increase our purification yield, and would also include adding washing and buffer steps. After this system has been set up, a DNA gel electrophoresis experiment can be run on the device flow-through to validate that biotinylated DNA can be captured using our microfluidic device design and the surface functionalization protocol used works as expected.

Once these have been validated the next step would be to quantify the devices performance, and compare the amount of cells needed to provide a sufficient DNA sample via Femto-seq, and determine the reduction of cells needed for this process from the beginning of the summer, which was 30,000 cells, to now. Next, elution steps to break the strepatavidin-biotin complex formed in this device should be tested and optimized.

The goal is to find a protocol that does minimal damage to the device itself to encourage longevity of the materials used. Part of this elution step would be to develop a flow-through collection protocol that leads to minimal loss of the DNA we worked so hard to affinity capture in the channel. Furthermore, ideally after the steps to optimize this device's function have been established, the system to control the device itself should become programmable, to make device operation as automatic as possible.

References:

[1]   Ma, S. et al. 2018. Sci. Adv. 4(4).

[2]   Stroock, A.D. et al. 2002. Science 295, 647-51.

Antiperovskite Thin Films Grown by Plasma-Assisted Molecular Beam Epitaxy

Madison Miller

Materials Science and Engineering, University of Florida

Abstract:

Antiperovskite crystals are of increasing interest in the semiconductor industry because of their narrow bandgap and potential to be used for near infrared applications. These crystals have the same structure as perovskites, but the positions of the cations and anions are switched; this results in a stoichiometry of R_3MO where R is an alkali earth element and M is a metal [1]. Current material options for near-infrared semiconductor devices are all toxic, which is not ideal for potential biomedical applications. Ca_3SiO is a nontoxic antiperovskite that has a narrow, direct bandgap and is a near infrared semiconductor that could replace current toxic options. However, thin film fabrication of this material must be improved before the use of Ca_3SiO in near infrared devices can be realized.

Introduction:

The goal of this project was to use plasma-assisted molecular beam epitaxy (PA-MBE) to grow Ca_3SiO thin films, determine ways to control the Ca/Si composition of the films, and determine the crystal orientation and crystallinity of the Ca-Si-O thin films grown using PA-MBE. Twenty thin films were deposited on $SrTiO_3$ (100) substrates over a range of Ca temperatures, and each film was capped using Al_2O_3 that was also deposited using PA-MBE. The films were then characterized using X-ray photoelectron spectroscopy (XPS), X-ray diffraction (XRD), and X-ray fluorescence (XRF). It was found that the Ca/Si beam equivalent pressure (BEP) ratio could be used to tune which Ca-Si-O phase was deposited, and CaO is preferentially formed due to the high concentration of Ca. One of the samples had the desired Ca_3SiO composition, while the rest of the films contained other phases such as $CaSiO_3$ and Ca_2SiO_4. The Al_2O_3 capping layer was found to be effective in protecting the Ca_3SiO from reacting with air. Future goals include improving the reproducibility of Ca_3SiO formation as well as optical and electrical transport characterization of these films.

Summary of Research:

First, the $SrTiO_3$ (100) substrates were annealed at 1100°C in air to create an atomically flat surface for the film to be deposited on. Atomic force microscopy was used to verify that the substrate surface was atomically smooth. Then, PA-MBE of Ca and Si was conducted for two hours with the substrate temperature set at 900°C. The silicon cell temperature was kept constant for all samples, while a range of temperatures between 400 and 600°C were tested for the calcium cell. The BEP ratios for the range of Ca temperatures tested are shown in Figure 1. Oxygen was flowed in the chamber and the partial pressure ranged between 0.5 and 3.0 × 10^{-5} torr during the deposition process for each sample. After this deposition, the substrate temperature was lowered to approximately 100°C and Al deposition was conducted for two hours to form an Al_2O_3 capping layer. The temperature of the Al cell was 850°C. Each sample was then characterized using XRD, XRF, and XPS to determine the composition and structure of the films.
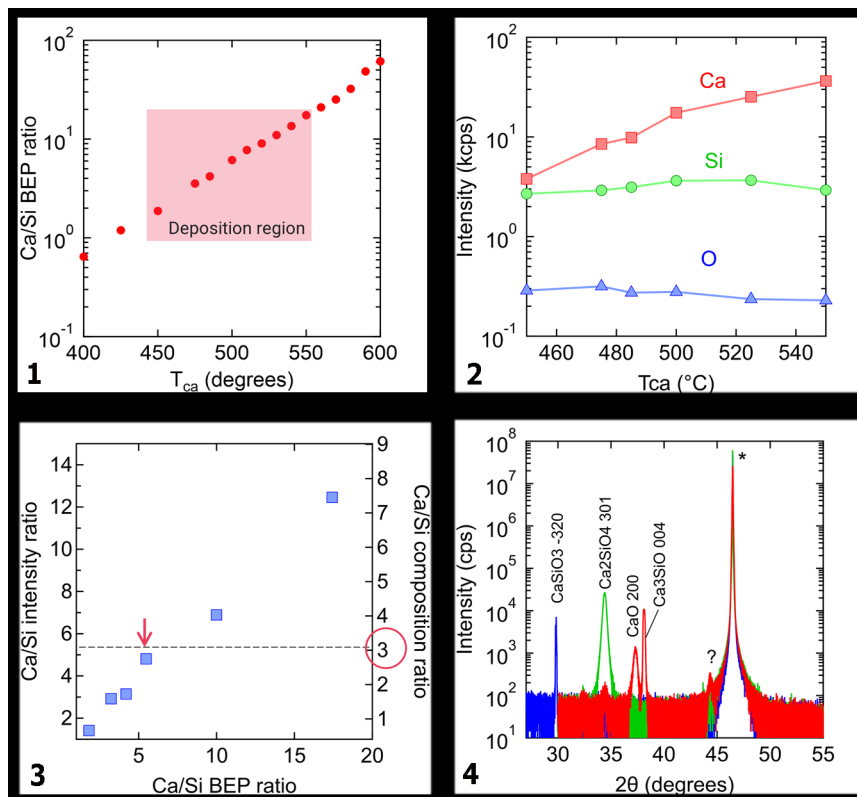
*Figure 1, top left: A plot showing the Ca/Si beam equivalent pressure (BEP) ratios for the Ca temperature range used for deposition, which is indicated by the red box. The Si temperature remained constant. Figure 2, top right: Intensity vs calcium deposition temperature for Ca, Si, and O, taken using XRF. Figure 3, bottom left: A plot showing the Ca/Si composition ratios for each Ca/Si BEP ratio used for sample deposition. The ideal Ca/Si composition ratio is 3, and the sample closest to this ratio is indicated by the red arrow. Figure 4, bottom right: A high-resolution XRD scan of three samples deposited at different Ca/Si BEP ratios. The peak labeled with * is a characteristic peak of the $SrTiO_3$ substrate.*

Conclusions and Future Steps:

The XRF measurements collected for the samples confirmed that the calcium intensity increases as the Ca temperature increases, which is shown in Figure 2. The Si and O intensity was relatively constant across all samples since the growth parameters for these two materials were kept constant. For the desired Ca_3SiO film, the ideal Ca/Si composition ratio should be 3. A wide range of Ca/Si ratios were measured for the samples as can be seen in Figure 3. By looking at this data it can be seen that the composition ratio changes as the Ca/Si BEP ratio changes. A Ca/Si BEP ratio of 5.5 resulted in a sample with a nearly ideal composition ratio of 3. This film was also the only sample that had a Ca_3SiO peak in its XRD spectrum. The characteristic peaks for the Ca-Si-O compounds present in the films are within the 25° to 55° region of the XRD spectrum; a high-resolution scan of this region for three different samples is shown in Figure 4. The three samples shown in this spectrum are characteristic of all of the films, as they show the three primary stoichiometries found in the samples: $CaSiO_3$, Ca_2SiO_4, and Ca_3SiO. There were also CaO peaks present in most of the sample spectra, which is due to a high concentration of Ca in the sample.

The presence of different Ca-Si-O phases for different deposition conditions indicates the Ca/Si BEP ratio could be used to tune the phase of the final film. However, this relationship will need to be further studied since only one film had the desired Ca_3SiO structure despite multiple samples being deposited at the ideal 5.5 Ca/Si BEP ratio. In addition, Ca_3SiO is known to be reactive in air, so the effectiveness of the Al_2O_3 capping layer was tested by conducting XRD again one month after depositing the film. There were no changes in the XRD spectrum, which indicates that aluminum oxide is effective at protecting the Ca_3SiO phase in air.

The relationship between the Ca/Si BEP ratio and Ca/Si composition needs to be further investigated to improve the reproducibility of Ca_3SiO formation. Future deposition processes can be conducted at different substrate temperatures, Si flux, or different oxygen content to better tune the composition of the final films. Another area of interest is optical and electrical transport characterization for these films.

References:

[1]   Quintela et al., Sci. Adv. 2020; 6 : eaba4017.

Development of Pi-Conjugated Molecular Assemblies towards Chiral Amine Sensing

Matthew Po

Chemical Engineering, University of Florida;
Chemical and Biomolecular Engineering, University of California, Berkeley

2022 Cornell NanoScale Science & Technology Facility
International Research Experiences for Undergraduates (CNF iREU) Program

CNF iREU Principal Investigator: Masayuki Takeuchi,
National Institute of Material Science (NIMS), Tsukuba, Ibaraki, Japan

CNF iREU Mentor: Atsuro Takai, NIMS, Tsukuba, Ibaraki, Japan

Primary Source(s) of Research Funding: 2022 CNF iREU Program via NSF grant NNCI-2025233

Contact: matthew.po@berkeley.edu, TAKEUCHI.Masayuki@nims.go.jp, TAKAI.Atsuro@nims.go.jp

Website: https://cnf.cornell.edu/education/reu/2022

Abstract:

Due to the functional implications of an amine's chirality, there is significant interest in methods for sensing amine chirality. Current methods of chiral amine sensing typically involve large, high-cost instruments whose operation can be time consuming. Our previous work has demonstrated the catalyst-free click reaction between alkynyl-substituted Pi(π)-extended electron acceptors such as perylene diimide and amines [1]. In this work, the capability to perform chiral amine sensing using supramolecular assemblies of such alkynyl-substituted π-extended electron acceptors was investigated. Herein, the synthesis of a novel perylene diimide compound and characterization of its supramolecular assembly process is reported. Further, preliminary kinetic studies of click reactions between the developed assemblies and chiral amines indicates its potential use for chiral amine sensing.

Summary of Research:

An amine's chirality can have dramatic impacts on its functionality; for example, one enantiomer of a chiral amine may have useful medical applications, while the other may be biologically inactive. Thus, chiral amine sensing is important for verifying whether only the desired enantiomer is present in a sample. Methods such as high-performance liquid chromatography with a chiral column, circular dichroism, and nuclear magnetic resonance with chiral reagents are the major current methods that are currently used to perform such sensing; however, these methods rely on large, expensive machinery and can be time consuming. Thus, an inexpensive, facile method of chiral amine sensing is highly desired.

A potential method of achieving this relies on the reactivity of amines. Amines have been shown to undergo a catalyst-free click reaction with alkynyl-substituted π-extended electron acceptors such as naphthalene diimide (NDI) and perylene diimide (PDI) [1]. Such alkynyl-substituted NDI and PDI compounds can be formed into supramolecular assemblies whose conformation is dictated by "assembling units" that are side chains at the imide positions [2]. Through
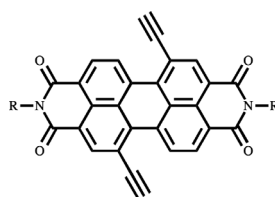

Figure 1: Structure of R-PDI2.

selection of a chiral assembling unit, a chiral supramolecular assembly can be produced that may potentially demonstrate enantioselectivity in reactions with chiral amines. Such chiral supramolecular assemblies can then be used as chiral amine sensors based on the differing kinetics that result from the enantioselectivity of the reaction.

In this work, a novel alkynyl-substituted PDI compound with chiral side chains (R-PDI2) was synthesized. The particular side chains used and synthetic scheme will not be reported here, but the general structure of the compound can be found in Figure 1. After synthesis of R-PDI2, the supramolecular assembly process was characterized using temperature-dependent ultraviolet-visible (UV-vis) absorption spectroscopy to optimize the solvent conditions for formation of supramolecular assemblies. To visualize the morphology of these assemblies, atomic force microscopy (AFM) images were taken of the compound after the assembling process. Finally, kinetic studies of the reactions of these supramolecular assemblies with enantiomers of a chiral amine were performed using time-dependent UV-vis absorption spectroscopy.
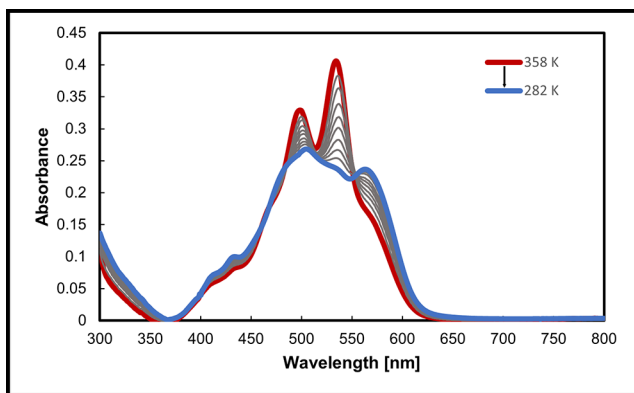
Figure 2: Temperature-dependent UV-vis absorption spectral changes for R-PDI2 (20 µm) in MCH/p-xylene (1:1 v/v) during cooling from 358 K to 282 K at a rate of 1 K/min.
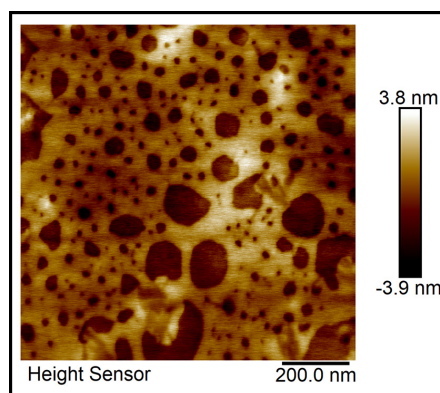

Figure 3: AFM image of a spin-coated sample prepared by cooling R-PDI2 (20 µm) from 358 K to 283 K at 1K/min in MCH/p-xylene (1:1 v/v).

Results:

Assembly Characterization. To optimize the solvent system for the supramolecular assembly process, UV-vis absorption spectroscopy measurements were taken over a range of temperatures in different solvent mixtures. The goal was to find a solvent in which 1) a significant change in the UV-vis absorption spectra could be observed across the range of temperatures and 2) the assemblies did not precipitate from solution up to a monomer concentration of 25 ?M. This was achieved in a 1:1 v/v mixture of methylcyclohexane (MCH) and *p*-xylene. The UV-vis absorption spectra demonstrating this assembly process can be seen in Figure 2.

Visualization of the assembly structure was achieved through AFM measurement of a sample spin-coated from 1:1 v/v MCH/*p*-xylene. A resulting AFM image can be seen in Figure 3. The AFM image reveals the formation of thick fibers in a porous sheet, indicating that the monomers are assembling into stacked monomer chains.

Reactions with Chiral Amines. To determine whether supramolecular assemblies of R-PDI2 could be used to differentiate between amine enantiomers, preliminary kinetic studies were performed using time-dependent UV-vis absorption spectroscopy. R-PDI2 assemblies (18.75 µm) were reacted with (R)- and (S)-1-phenylethylamine (0.49 µm) over the course of 24 hours. Changes in the absorbance at 512 and 700 nm were used to qualitatively demonstrate differences in reaction kinetics between the (R)- and (S)-enantiomers of 1-phenylethylamine. Plots of the absorbance at 512 and 700 nm can be found in Figure 4. The spectral analysis indicates that the reaction kinetics of R-PDI2 are slightly different depending on the enantiomers.

Conclusions and Future Steps:

This work demonstrates the potential application of supramolecular polymers of an alkynyl-substituted PDI for chiral amine sensing. The novel compound R-PDI2 was successfully synthesized, assembled, and characterized, allowing for its use in future work.

Further, preliminary kinetic studies revealed that there is some degree of stereoselectivity involved in reactions between R-PDI2 assemblies and chiral amines. However, further work must be done to improve the application of these materials, with the ultimate goal of being able to react such an assembly with chiral amines and observe a color change that requires no instrumentation to detect. Finally, another promising direction of this work is to investigate R-PDI2's application for sensing chiral diamines, which would likely experience greater stereoselectivity due to crosslinking between R-PDI2 monomers.

References:

[1] Takai and M. Takeuchi, Bulletin of the Chemical Society of Japan, vol. 91, no. 1, pp. 44-51, 2018.

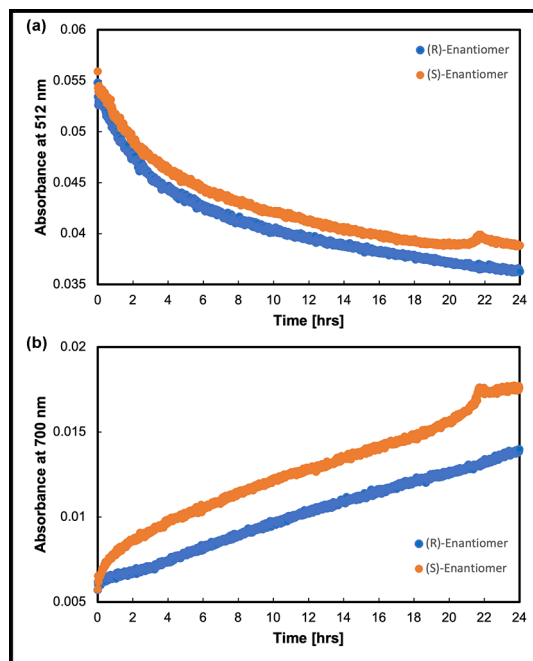[2] M. Tan, M. Takeuchi and A. Takai, Chemical Science, vol. 13, no. 15, pp. 4413-4423, 2022.

Figure 4: Absorbance values at (a) 512 nm and (b) 700 nm over the course of 24 hours for the reaction of R-PDI2 assemblies with the two enantiomers of 1-phenylethylamine.

Investigating the Electrokinetic Behavior of Cement-Based and Alternative Cementitious Materials

Rachel Qian

Chemical Engineering, Villanova University

2022 Cornell NanoScale Science & Technology Facility Research Experiences for Undergraduates (CNF REU) Program

CNF REU Principal Investigator: Dr. Sriramya Nair, Civil and Environmental Engineering, Cornell

CNF REU Mentor: Lyn Zemberekci, Civil and Environmental Engineering, Cornell University

Contact: rqian@villanova.edu, sn599@cornell.edu, lz549@cornell.edu

Website: https://cnf.cornell.edu/education/reu/2022

Abstract:

Portland cement production is a major contributor of carbon dioxide emissions, The need to incorporate large amounts of Supplementary Cementitious Materials (SCMs) to reduce the carbon footprint arises. Various SCMs were dispersed in diluted pore solutions that mimic native pore solutions of cement pastes characterized by their high pH and ionic nature. Chemical additives such as sodium glucoheptonate retarders and naphthalene sulfonate-based superplasticizers were employed to track their efficacy with the SCMs. Electrokinetic properties such as zeta potential was of primary interest in this study to ensure cement pastes have adequate rheological properties. Factors that influenced zeta potential such as electrical conductivity and pH were also measured in optimized particle solid concentrations. Stable zeta potentials have an absolute value measurement of 30 mV or above. Without the use of admixtures, it was found that majority of the particles were unstable and tended to aggregate in the pore solutions, with zeta potential values ranging from –3.13 mV to 11.5 mV. Silica flour displayed the most stable behavior in the diluted pore solution concentration, with a zeta potential around –22 mV. The use of chemical additives led to increases in the zeta potential values as compared to those of the neat particles, demonstrating that the additives are compatible with some of the particles and effective in improving the stability of the solution. Furthermore, scanning electron microscope imaging was used to view the shape and size of the cementitious particles as these factors also affect the rheology of the cementitious paste.

Summary of Research:

This research aimed at characterizing the electrokinetic behavior of Supplementary Cementitious Materials (SCMs), such as silica flour (SFL), class F fly ash (FAF), class C fly ash (FAC), metakaolin (MK) and ground granulated blast-furnace slag (SLAG) in DI water and pore solutions. Additionally, class H cement (CEM-H) was also analyzed as a baseline.

To study the electrokinetic behavior, zeta potential values were tracked using a zetasizer, Malvern Instrument. 800 µL of these neat (in the absence of chemical additives) pore solutions was injected into a reusable cuvette, which was then placed into the zetasizer. The zetasizer measured the sample's electrophoretic mobility at six measurements per sample and used the Smoluchowski approach to calculate the zeta potential values.

We found that SFL had most stable behavior in DI water, with zeta potential values above 30 mV for all concentrations. FAC experienced aggregation, which was attributed to the pH and conductivity of the solution. After graphing zeta potential vs conductivity, it was found that as conductivity increased, the zeta potential decreased, and solutions became less stable. These trends are summarized in Figure 1.

Then we used a synthesized pore solution made up of 0.6 g/L calcium sulfate dehydrate, 5.2 g/L sodium hydroxide, 17.9 g/L potassium hydroxide, and 2.4 g/L calcium hydroxide with a pH of 13.5 to test our SCMs and class H cement particles. Pore solution concentration used was 25 mL pore solution / 375 mL DI water. We mixed 100 mL of this diluted solvent with 100 mg
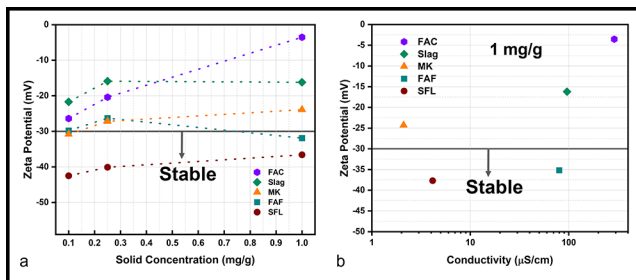
Figure 1: (a) Zeta potential values of various SCM particles with increasing solid concentration in deionized water, (b) Zeta potential vs conductivity for one concentration.

Particle	Zeta Potential (mV)	pH	Conductivity (mS/cm)
Class H Cement (CEMH)	4.5	12.4	7.5
Silica Flour (SFL)	-22.0	12.2	7.2
Class F Fly Ash (FAF)	-3.1	12.1	6.9
Metakaolin (MK)	1.4	12.1	7.6
Class C Fly Ash (FAC)	2.2	12.1	6.8
Slag	12.0	12.2	8.0

Table 1: Electrokinetic behavior of various SCMs and class H cement in pore solution.
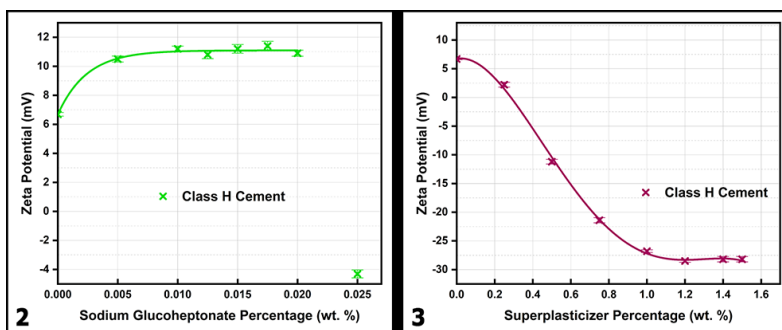
Figure 2, left: Zeta potential values of class H cement in pore solution with an increasing content of the retarder sodium glucoheptonate. Figure 3, right: Zeta potential values of class H cement in pore solution with an increasing content of the naphthalene-based superplasticizer.

particles through a 15-minute sonication. As shown in Table 1, it was found that majority of the particles became unstable and tended to aggregate in the pore solutions, with zeta potential values ranging from –3.13 mV to 11.5 mV. SFL displayed the most stable behavior in the diluted pore solution concentration, with a zeta potential around –22 mV. The use of chemical additives such as sodium glucoheptonate (SGH) and naphthalene-based superplasticizers led to increases in the zeta potential values of the CEM-H as compared to those without any additives, demonstrating that the additives are compatible and effective in improving the stability of the solution. However, these increases were bounded by certain concentrations of additives. This is illustrated in Figures 2 and 3.

Conclusions:

Zeta potential values of SCMs such as MK and FAF were similar to those found in literature [1-3], validating the procedure of this study. Majority of SCMs exhibited stable behavior when using deionized water as a solvent, apart from FAC. Opposite was true when using pore solution as a solvent, except for SFL. CEM-H interactions with the retarding additive SGH in the pore solution indicated that this additive improves the stability of the solution to a certain point, after which increasing the SGH content

results in aggregation. CEM-H in the presence of the superplasticizer additive showed that stability of the solution increased up to a saturation point, after which there is no significant effect.

Future Steps:

To observe aggregation of particles, along with measuring zeta potential we will also measure the particle size of each of the SCMs. This will be achieved by adding an additional sieving and filtering process to limit particle sizes to 5 μm. We will also aim at conducting adsorption tests of polymer-based additives onto the SCM particles using an ultraviolet-visible (UV-vis) light device. In future experiments, there will be further optimization of pH and conductivity versus zeta potential.

References:

[1]   Malta, J. O., Oliveira, L. V., Ueki, M. M., and Barreto, L. S. (2021). Characterization and stabilization of nano-metakaolin colloidal suspensions. Powder Technology, 383, 43-55.

[2]   Malek, R. I., Khalil, Z. H., Imbaby, S. S., and Roy, D. M. (2005). The contribution of class-F fly ash to the strength of cementitious mixtures. Cement and concrete research, 35(6), 1152-1154.

[3]   Wang, C., Kayali, O., and Liow, J. L. (2021). The effectiveness and mechanisms of superplasticisers in dispersing class F fly ash pastes. Powder Technology, 392, 81-92.

How the Band Structure of Graphene/Nanomesh Bilayers Depends on its Stacking Symmetry

Veronica Show

Chemistry, Harvey Mudd College

Abstract:

Here, we explore a bilayer system which includes graphene and a graphene nanomesh with a potentially tunable bandgap. Using computational methods, we find that the behavior of the system is similar to a superposition of the two monolayers. Additionally, we find that the stacking symmetry of the system affects its band structure; AA graphene/nanomesh bilayers exhibit semiconductor behavior whereas AB graphene/nanomesh bilayers exhibit conductor behavior.

Introduction and Methods:

Graphene has become a material of interest in the past few years due to its unique band structure features. Its Dirac cone band structure (as shown in red in Figure 1 at the Γ point) makes it an effective conductor. Additionally, Du, et al., found that introducing pores into graphene, such as the one shown boxed in blue in Figure 1, causes a direct band gap opening of 3.2 eV [1].

Recent efforts to synthesize these nanomeshes have been successful using bottom-up polymerization methods [2]. Due to its physical and electronic structure, graphene nanomeshes have potential application in many fields including phonon control, hydrogen storage, and water filtration. Additionally, when two of these sheets are stacked with any lattice constant mismatch or angle mismatch, it results in large-scale interference patterns, or moiré lattices. In a moiré lattice, the overall structure is periodic with many local differences.

Two regions of significance can be defined as an AA stacked region, where two layers are aligned so every carbon atom is directly on top of another carbon atom, and an AB stacked region, where two layers are staggered so the top layer is shifted along the diagonal of the nanomesh unit cell by exactly one side length of the hexagon. This difference in structure can result in unique electronic behavior which could indicate that electrons can be localized to certain regions of the moiré lattice.

Calculations were completed using GGA functionals in Quantum Espresso, an open-source program which calculates the electronic properties of nanoscale materials using density functional theory, pseudopotentials and plane waves [3,4]. The crystal structure of the materials was visualized using XCrysDen [5,6].

Results and Discussion:

First, the crystal structure for a graphene monolayer and the graphene nanomesh (shown boxed in blue in Figure 1) monolayer were optimized. The unit cell of graphene was found to have a lattice constant of 2.464 Å (7.3920 Å for the 3×3 supercell), and the unit cell of the graphene nanomesh was found to have a lattice constant of 7.5115 Å. Using these optimized structures, the band structure for both monolayers were calculated. The graphene band structure (using the 3×3 supercell to have symmetry with the nanomesh) contains the distinctive Dirac cone at the Γ point, and the band gap of the nanomesh is found to be 2.4021 eV. This band gap is much less than literature values [1], but this is due to GGA being used, which is known to underestimate band gaps, whereas HSE06 was used in literature calculations, which usually gives more accurate results. The overall shape of the band structures for both the graphene and nanomesh monolayers match literature results [1,7].

Using the optimized monolayer structures, AA and AB bilayers were approximated by stacking one nanomesh monolayer on one graphene monolayer with the nanomesh lattice constant and a bilayer distance equal to bilayer graphene, shown in the inserts of Figure 2 and 3 respectively. Using these unit cells, the band structure for each bilayer was calculated, as shown in Figure 2 and 3 for AA and AB respectively. There are many similarities in the band structures of the bilayers and the superposition of the 3×3 graphene supercell and the graphene nanomesh, especially for AB. Specifically, the band gap at the K point and curve at the Γ point appear in both the AA and AB band structures. Additionally, the Dirac cone of the 3×3 supercell at the Γ point is observed exactly in the AB band structure. In the AA band structure, the feature is similar, but it also has a band gap opening of 0.0557 eV. This is significant because it indicates that while the structures are very similar, the AB bilayer behaves like a conductor whereas the AA bilayer behaves like a semiconductor.

Conclusions and Future Steps:

In conclusion, the band structure of a graphene/nanomesh bilayer depends on its stacking symmetry: the AA bilayer has a direct band gap and the AB bilayer has a Dirac cone. This difference suggests in a moiré lattice, electrons will be confined to the AB, or conductive, regions. Further work is needed to fully model the moiré lattice and determine what relaxation effects may occur when stacking the two layers. Additionally, further research consists of determining the band structure of these bilayers with different types of nanomeshes, including changes in pore size and distance between pores.

Acknowledgments:

References:

[1]   Du, A., et al., JACS Comm., 2010, 132, 2876-2877, 10.1021/ja100156d.

[2]   Bieri, M., et al., RCS Chem. Comm., 2009, 45, 6919-6921.

[3]   Giannozzi, P., et al., J.Phys.:Condens.Matter, 2009, 21, 395502.

[4]   Giannozzi, P., et al., J.Phys.:Condens.Matter, 2017, 9, 465901.

[5]   Kokalj, A., Comp. Mater. Sci., 2003, 28, 155-168.

[6]   Kokalj, A., J. Mol. Graphics Modelling, 1999, 17, 176-179.

[7]   Newson, Ryan. 2010. Dynamics of Carriers and Photoinjected Currents in Carbon Nanotubes and Graphene.

Figure 1, top: Superposition of a graphene monolayer and a nanomesh monolayer. Many of the prevalent features — such as the Dirac cone of graphene at the Γ point and the band gap in the nanomesh at the K point — are observed in both bilayer band structures, especially for AB stacking.

Figure 2, middle: Calculated band structure for the AA stacked graphene/nanomesh bilayer. It exhibits a band gap of 0.0557 eV at the Γ point.

Figure 3, bottom: Calculated band structure for the AB stacked graphene/nanomesh bilayer. It exhibits a Dirac cone at the Γ point. Its features are very similar to the superposition of the graphene and nanomesh monolayers, especially the Dirac cone of the graphene at the Γ point and the band gap of the nanomesh at the K point.
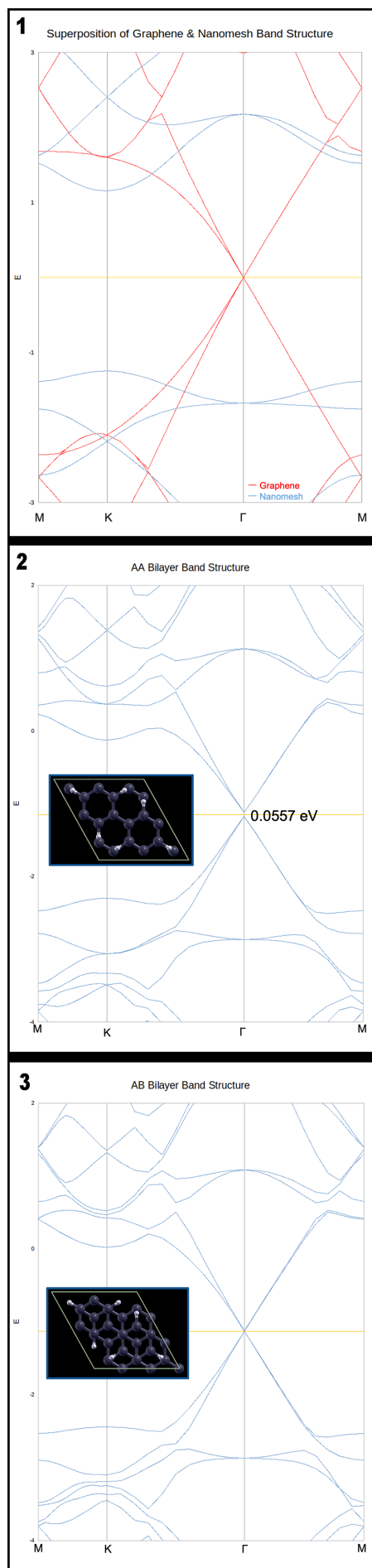
You Will Ru(e) the Day: Developing Area-Selective Processes to Enable Ru-Based Interconnect at the 2 nm Node and Beyond

Elisa Simoni

**Engineering Physics and Electrical Engineering,
Rose-Hulman Institute of Technology**

Abstract:

For many years, scientists have used photolithography to layer patterns onto wafers. However, the minimum size of the features on the patterns is limited by the wavelength of the light used. Now, as the electronics industry seeks to create single digit nanometer features, photolithography is reaching the limits of its capabilities; a new method for patterning substrates is needed. One such way is through selective deposition of materials in which deposition is determined by the surface chemistry. In atomic layer deposition (ALD), a film is typically grown using half reactions in an AB cycle. First, the precursor (A) binds the substrate. Then, the co-reactant (B) reacts on the surface with the precursor to grow the desired film. Each AB cycle results in a film growth thickness of approximately one angstrom [1]. Because the user controls the number of cycle repetitions, thickness can be tailored with high precision. For area-selective ALD, if a chemical (co-adsorbate) is introduced before and alongside the precursor, the co-adsorbate can attach to certain surfaces and block film growth in order to achieve selectivity [2]. Additionally, the typical material used for electrical interconnects is copper. However, for single digit nanometer features, Ruthenium is a better conductor. Overall, the purpose of this project is to create different sized line-and-space patterns of alternating Ruthenium and dielectrics (Al_2O_3 and SiO_2) using a lift-off process. These patterns can then be used to test which co-adsorbates provide the best selectivity given the metals and dielectrics used in the patterns.

Summary of Research:

Ten 100 mm silicon wafers were utilized to create the patterns. First, all wafers were cleaned using an RCA clean. A 200 nm film of SiO_2 was thermally grown on five of the wafers using an oxidation furnace. A 50 nm film of Al_2O_3 was deposited via ALD on the other wafers using the Veeco Savannah and the Oxford ALD FlexAL. The negative photoresist nLOF2020 was spun on each wafer at 3000 rpm for one minute, followed by a one-minute bake. A GDSII file containing line-and-space patterns of 100, 30, 10, 3, and 1 μm was created using the gdstk python library and then used along with the Heidelberg Mask Writer DWL2000 to create the mask pattern. Each wafer was then exposed using the ABM contact aligner, baked on a hotplate for one minute, and developed in the Hamatech Wafer Processor. The SC4500 Evaporator was used to deposit the metals. Five nm of titanium was first deposited to help the ruthenium stick to the wafer. Then, 20 nm of ruthenium was deposited. After stripping the photoresist, the pattern was then examined using atomic force microscopy (the AFM).
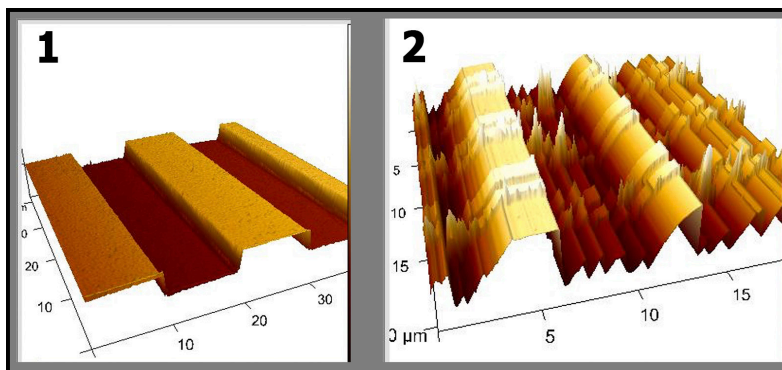
Figure 1: 10 μm line-and-space pattern. Figure 2: 3 μm line-and-space pattern.

Overall, the 100, 30, and 10 μm lines had good coverage and little surface roughness. However, there were holes and significantly more roughness in the 3 and 1 μm lines. This can be seen in the AFM images of the 10 μm and 3 μm lines as shown in Figures 1 and 2. This is likely due to the wafer not being clean enough before undergoing the photolithography process. Therefore, the 100, 30, and 10 μm lines can now be utilized for area-selective depositions.

References:

[1] S. M. George, "Atomic Layer Deposition: An Overview," ACS Publications, Nov. 30, 2009. https://pubs.acs.org/doi/pdf/10.1021/cr900056b (accessed Aug. 13, 2022).

[2] T. Suh et al., "Competitive Adsorption as a Route to Area-Selective Deposition," ACS Appl. Mater. Interfaces, vol. 12, no. 8, pp. 9989–9999, Feb. 2020, doi: 10.1021/acsami.9b22065.

Index